



ATLAS NOTE

ATLAS-CONF-2016-050

August 4, 2016



Search for top squarks in final states with one isolated lepton, jets, and missing transverse momentum in $\sqrt{s} = 13$ TeV pp collisions with the ATLAS detector

The ATLAS Collaboration

Abstract

The results of a search for the stop, the supersymmetric partner of the top quark, in final states with one isolated electron or muon, jets, and missing transverse momentum are reported. The search uses the LHC pp collision data collected in 2015 and 2016 at a center-of-mass energy of $\sqrt{s} = 13$ TeV recorded by the ATLAS detector corresponding to an integrated luminosity of 13.2 fb^{-1} . The stop decay scenarios considered are those to a top quark and the lightest neutralino as well as to a bottom quark and the lightest chargino, followed by the chargino decays to the lightest neutralino and a W boson. A range of scenarios with different mass splittings between the stop, the lightest chargino and the lightest neutralino are considered. The analysis also targets the production of dark matter in association with a pair of top quarks using the same final state. The largest deviation from the Standard Model prediction is found in one of the seven signal selections, where 35 events are observed with 17 ± 2 background events expected, corresponding to a local significance of 3.3 standard deviations. A stop with a mass of 830 GeV decaying directly to a top quark and a massless neutralino is excluded at 95% confidence level. Stringent exclusion limits are also derived for all other considered stop decay scenarios, and upper limits are set on the visible cross-section for processes beyond the Standard Model. For the dark matter search, limits are obtained for the common coupling value of $g = 3.5$ in a plane of dark matter particle mass and a scalar or pseudo-scalar mediator mass. The maximal coupling of $g = 3.5$ is excluded at 95% confidence level for a scalar (pseudo-scalar) mediator mass up to 320 (350) GeV assuming a 1 GeV dark matter particle mass.

1 Introduction

Supersymmetry (SUSY) [1–6] is a well motivated extension of the Standard Model (SM) that introduces supersymmetric partner (superpartner) particles to each of the SM particles and that provides a natural solution [7, 8] to the hierarchy problem [9–12]. The top squark or stop (\tilde{t}), which is the superpartner of the top quark, is expected to be relatively light due to its large contribution to the Higgs boson mass radiative corrections [13, 14]. A common theoretical strategy for avoiding strong constraints from the non-observation of proton decay [15] is to introduce a multiplicative quantum number called R -parity. If R -parity is conserved [16], SUSY particles are produced in pairs and the lightest supersymmetric particle (LSP) is stable. This analysis follows the typical assumption that the lightest neutralino¹ ($\tilde{\chi}_1^0$) is the LSP. Since the $\tilde{\chi}_1^0$ interacts only weakly, it can serve as a candidate for dark matter [17, 18].

The analysis described in this note closely follows and extends the previous search for stop production using 2015 data [19]. This note presents a search targeting the direct production of the lighter stop² (\tilde{t}_1), illustrated by the diagrams in Figure 1. The stop can decay into a variety of final states, depending amongst other things on the SUSY particle mass spectrum, in particular on the masses of the stop, chargino and lightest neutralino. When the decay into $b\tilde{\chi}_1^\pm$ is kinematically allowed, the \tilde{t}_1 decay branching ratio (\mathcal{BR}) is determined by the stop mixing matrix and the field content of the neutralino/chargino sector.

In addition to the direct stop search, a dark matter (DM) scenario [20–22] is also studied. Figure 2 illustrates a Feynman diagram where the DM particles (represented by χ) are pair-produced via a spin-0 mediator (either scalar or pseudo-scalar). The mediator couples to the SM particles by mixing with the Higgs sector.

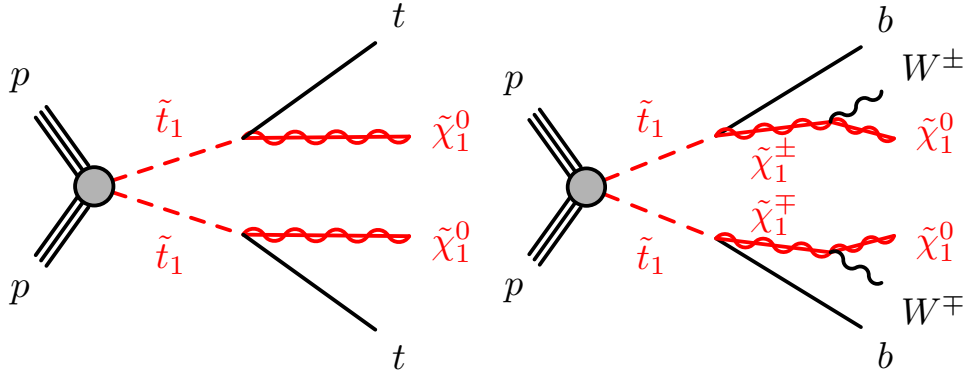


Figure 1: Diagrams illustrating the direct pair production of \tilde{t}_1 particles and their decays, which are referred to as $\tilde{t}_1 \rightarrow t + \tilde{\chi}_1^0$ (left) and $\tilde{t}_1 \rightarrow b + \tilde{\chi}_1^\pm$ (right). Furthermore, a mixed decay scenario where each \tilde{t}_1 decays via either $\tilde{t}_1 \rightarrow t + \tilde{\chi}_1^0$ and $\tilde{t}_1 \rightarrow b + \tilde{\chi}_1^\pm$ for various \mathcal{BR} is considered (not shown). For simplicity, no distinction is made between particles and antiparticles.

The analysis presented here targets final states with one lepton, where the W boson from one of the top quarks decays to an electron or muon (either directly or via a τ lepton) and the W boson from the other

¹ The charginos $\tilde{\chi}_{1,2}^\pm$ and neutralinos $\tilde{\chi}_{1,2,3,4}^0$ are the mass eigenstates formed from the linear superposition of the charged and neutral superpartners of the Higgs and electroweak gauge bosons (higgsinos, winos and binos).

² The superpartners of the left- and right-handed top quarks, \tilde{t}_L and \tilde{t}_R , mix to form the two mass eigenstates \tilde{t}_1 and \tilde{t}_2 , where \tilde{t}_1 is the lighter one.

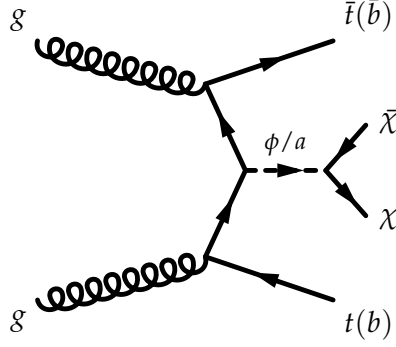


Figure 2: A representative Feynman diagram for s-channel spin-0 mediator production of dark matter particles.

top quark decays hadronically. The dominant SM background processes are: the production of $t\bar{t}$, the associated production of a top quark and a W boson (single top Wt), $t\bar{t} + Z(\rightarrow \nu\bar{\nu})$, and the associated production of W bosons and jets (W +jets). The search uses ATLAS data collected in proton-proton (pp) collisions in 2015 and 2016 corresponding to an integrated luminosity of 13.2 fb^{-1} at a center-of-mass energy of $\sqrt{s} = 13\text{ TeV}$. Previous searches for stop production have been carried out by ATLAS [19, 23–25] and CMS [26–31]. Searches for DM in association with heavy quarks have also been performed previously. The previous results were based on Effective Field Theory (EFT) models [32, 33], in contrast to the results reported here which are based on a Simplified model [21, 22].

This document is organized as follows. The ATLAS detector, dataset, and trigger are described in Section 2, and the corresponding set of simulated samples are detailed in Section 3. Section 4 presents the reconstruction and selection of physics objects and the definition of the discriminating variables. These variables are used in Section 5 to construct the signal event selections. The background estimation procedure and systematic uncertainties are described in Sections 6 and 7, respectively, and the results of this analysis are presented in Section 8. Section 9 contains concluding remarks.

2 ATLAS Detector and Dataset

The ATLAS detector [34] is a multipurpose particle physics detector with nearly 4π coverage in solid angle around the collision point.³ It consists of an inner tracking detector (ID), surrounded by a superconducting solenoid providing a 2 T axial magnetic field, a system of calorimeters, and a muon spectrometer (MS) incorporating three large superconducting toroid magnets. The ID provides charged-particle tracking in the range $|\eta| < 2.5$. During the LHC shutdown between Run 1 (2010–2012) and Run 2 (2015–), a new innermost layer of silicon pixels was added, which improves the track impact parameter resolution, vertex position resolution and b -tagging performance [35]. High-granularity electromagnetic and hadronic calorimeters cover the region $|\eta| < 4.9$. The central hadronic calorimeter is a sampling calorimeter with

³ ATLAS uses a right-handed coordinate system with its origin at the nominal interaction point (IP) in the center of the detector and the z -axis along the beam pipe. The x -axis points from the IP to the center of the LHC ring, and the y -axis points upwards. Cylindrical coordinates (r, ϕ) are used in the transverse plane, ϕ being the azimuthal angle around the z -axis. The pseudorapidity is defined in terms of the polar angle θ as $\eta = -\ln \tan(\theta/2)$. Angular distance is measured in units of $\Delta R \equiv \sqrt{(\Delta\eta)^2 + (\Delta\phi)^2}$.

scintillator tiles as the active medium and steel absorbers. All the electromagnetic calorimeters, as well as the endcap and forward hadronic calorimeters, are sampling calorimeters with liquid argon as the active medium and lead, copper, or tungsten absorber. The MS consists of three layers of high-precision tracking chambers with coverage up to $|\eta| = 2.7$ and dedicated chambers for triggering in the region $|\eta| < 2.4$. Events are selected by a two-level trigger system: the first level is a hardware-based system and the second is a software-based system.

The LHC collision data used in this analysis was collected during 2015 and 2016 and has a mean number of simultaneous pp interactions per bunch crossing, or “pileup”, of approximately 21.4 across the years. Following requirements based on beam and detector conditions and data quality, the dataset corresponds to an integrated luminosity of 13.2 fb^{-1} with an associated uncertainty of 2.1% and 3.7% in the 2015 and 2016 datasets respectively. The uncertainty is derived following the same methodology as that detailed in Ref. [36, 37]. Events used for this search were recorded using a trigger logic that accepts events with an E_T^{miss} threshold at trigger level of 80 GeV for the 2015 dataset and 100 GeV for the 2016 dataset. The trigger is more than 95% efficient for events passing an offline-reconstructed $E_T^{\text{miss}} > 200 \text{ GeV}$ requirement. An additional data sample used to estimate one of the background processes was recorded with a trigger requiring a photon with transverse momentum $p_T > 140 \text{ GeV}$, which is $> 99\%$ efficient for the offline photon selection described in Section 4.

3 Monte Carlo Simulations

Samples of Monte Carlo (MC) simulated events are used for the description of the background and to model the SUSY signals. Several matrix element (ME) generators are combined with parton shower (PS) and hadronization generators. Signal SUSY samples are generated at leading order (LO) with MG5_AMC@NLO v2 [38] and interfaced with PYTHIA 8 [39]. The \tilde{t}_1 decays are performed by PYTHIA and produce unpolarized top quarks. The $\tilde{\chi}_1^0$ is taken to be a pure bino. Background samples are generated with one of three setups:

- MG5_AMC@NLO v2 interfaced with PYTHIA 8 or Herwig++ using the CKKW-L [40] or the MC@NLO [41] method for matching a LO or next-to-leading-order (NLO) ME to the PS, respectively.
- POWHEG-Box v2 [42–46] interfaced to PYTHIA 6 [47] or Herwig++ using the POWHEG method [48, 49] for matching the NLO ME to the PS. Electroweak t -channel single top-quark events are generated using the POWHEG-Box v1 generator.
- SHERPA 2.1.1 and SHERPA 2.2 [50] using Comix [51] and OpenLoops [52] ME generators interfaced with the SHERPA parton shower [53].

The CT10 [54] NLO parton distribution function (PDF) set is used for ME calculations with POWHEG-Box and SHERPA 2.1.1. The NNPDF 3.0 NNLO [55] and NNPDF2.3 [56] PDF set are used for samples generated with SHERPA 2.2 and MG5_AMC@NLO, except for the NLO samples, which use either CT10 or NNPDF3.0 [55]. The CTEQ6L1 [57] LO PDF set along with the P2012 [58] set of underlying-event tuned parameters (UE tune) is used for PYTHIA 6; the NNPDF2.3 LO PDF set and the A14 UE tune [59] is used for PYTHIA 8; and the CT10 PDF set with the default UE tune provided by the authors of SHERPA is used for the SHERPA samples. The samples produced with MG5_AMC@NLO and POWHEG-Box use EVTGEN v1.2.0 [60] for the modeling of b -hadron decays. The simulation setup is summarized in Table 1

and more details can be found in Refs. [61–64] for $t\bar{t}$ and single top, W/Z +jets, dibosons, and $t\bar{t} + W/Z$, respectively. Additional samples aside from those shown in Table 1 are used to assess theoretical modeling uncertainties and are discussed in Section 7.

Process	ME generator	ME PDF	PS and Hadronization	UE tune	Cross-section order
$t\bar{t}$	POWHEG-Box v2	CT10	PYTHIA 6	P2012	NNLO+NNLL [65–70]
Single top	POWHEG-Box v1/v2	CT10	PYTHIA 6	P2012	NNLO+NNLL [71–73]
W/Z +jets	SHERPA 2.2	NNPDF3.0 NNLO	SHERPA	Default	NNLO [74]
Diboson	SHERPA 2.1.1	CT10	SHERPA	Default	NLO
$t\bar{t} + W/Z$	MG5_AMC@NLO 2.2.2	NNPDF2.3	PYTHIA 8	A14	NLO [38]
$t\bar{t} + \gamma$	MG5_AMC@NLO 2.2.3	CTEQ6L1	PYTHIA 8	A14	NLO [38]
$W + \gamma$	SHERPA 2.1.1	CT10	SHERPA	Default	LO
SUSY signal	MG5_AMC@NLO 2.2.2	NNPDF2.3	PYTHIA 8	A14	NLO+NLL [75]
DM signal	MG5_AMC@NLO 2.2.2	NNPDF3.0 LO	PYTHIA 8	A14	LO

Table 1: Overview of the nominal simulated samples.

Signal samples of unpolarized top squark–antisquark pairs are generated with different stop decay and mass configurations. The first scenario assumes the $\tilde{t}_1 \rightarrow t + \tilde{\chi}_1^0$ decay with a branching ratio (\mathcal{BR}) of 100%. Samples are generated in a grid across the plane of \tilde{t}_1 and $\tilde{\chi}_1^0$ masses with a spacing of 50 GeV for most of the plane; the grid is more finely sampled towards the diagonal region where $m_{\tilde{t}_1}$ approaches $m_t + m_{\tilde{\chi}_1^0}$. The second signal scenario assumes the $\tilde{t}_1 \rightarrow b + \tilde{\chi}_1^\pm \rightarrow bW^{(*)}\tilde{\chi}_1^0$ decay with a \mathcal{BR} of 100%. The three-dimensional parameter space of the \tilde{t}_1 , $\tilde{\chi}_1^\pm$, and $\tilde{\chi}_1^0$ masses is probed using the two-dimensional plane of \tilde{t}_1 and $\tilde{\chi}_1^0$ masses under two different assumptions. In the first plane, the chargino mass is set to twice the LSP mass ($m_{\tilde{\chi}_1^\pm} = 2m_{\tilde{\chi}_1^0}$), motivated by the pattern in GUT-scale models with gaugino universality. In the second plane, the chargino mass is set to be slightly below the stop mass, $m_{\tilde{\chi}_1^\pm} = m_{\tilde{t}_1} - 10$ GeV.

The DM signal samples are generated with MG5_AMC@NLO according to the diagram described in Figure 2. The model has 5 free parameters corresponding to the masses of the mediator and dark matter particle, the coupling of the mediator with the dark matter and SM particles, and the width of the mediator. The signal grid is generated by scanning over the mass parameters. The coupling of the mediator to the dark matter particle (g_χ) is set to be equal to its coupling to the quarks (g_q). The common coupling is allowed to vary in the range 0.1–3.5. The minimal width assumption is made for the mediator [21].

All the MC samples are normalized to the highest-order (in α_S) cross-section available, as indicated in the last column of Table 1. The cross-sections for the pair and single production of top quarks as well as for the signal processes also include resummation of soft gluon emission to next-to-next-to-leading-logarithmic (NNLL) and next-to-leading-logarithmic (NLL) accuracy, respectively. The W/Z +jets samples have been produced with a simplified scale setting prescription in the multi-parton matrix elements, to improve the event generation speed. A theory-based re-weighting of the jet multiplicity distribution is applied at event level, derived from event generation with the strict scale prescription. As described in Section 6.1.3, it is important that the simulated $t\bar{t} + \gamma$ and $t\bar{t} + Z$ events are as similar as possible. Therefore, a small 4% correction is applied to the $t\bar{t} + \gamma$ cross-section to account for a different PDF set, factorization/renormalization scale, and number of partons from the matrix element.⁴ The same NLO

⁴ The $t\bar{t} + \gamma$ sample uses a fixed factorization/renormalization scale of $2 \times m_{\text{top}}$ with no extra partons in the ME. The $t\bar{t} + Z$ sample uses the default $\sum m_T$ scale and is generated with up to two partons. The top decay is performed in MG5_AMC@NLO for $t\bar{t} + \gamma$ to account for hard photon radiation from the top decay products, which is a $\sim 10\%$ effect for $p_T^\gamma \sim 145$ GeV [76].

QCD K -factor is then applied to the $t\bar{t} + \gamma$ process as is used for the $t\bar{t} + Z(\rightarrow \nu\bar{\nu})$ process [38].⁵ The cross-sections for the $t\bar{t}$, W +jets, and single top processes are used for cross-checks and optimization studies, while for the final results these processes are normalized to data in control regions.

All background samples, except for the $t\bar{t} + \gamma$ sample, are processed with the full simulation of the ATLAS detector [77] based on GEANT 4 [78]. The signal samples and the $t\bar{t} + \gamma$ sample are processed with a fast simulation [79] of the ATLAS detector with parameterized showers in the calorimeters. All samples are produced with varying numbers of simulated minimum-bias interactions generated with PYTHIA 8 overlaid on the hard-scattering event to account for pileup from multiple pp interactions in the same or nearby bunch crossings. The average number of interactions per bunch crossing is reweighted to match the distribution in data. Furthermore, the simulated samples are reweighted to account for small differences in the efficiencies of physics-object reconstruction and identification with respect to those measured in data.

4 Event Reconstruction and Selection

In this analysis, physics objects are labeled as either *baseline* or *signal* depending on various quality and kinematic requirements, where the latter label describes a tighter selection of the former. Baseline objects are used to distinguish between the physics objects in the event and to compute the missing transverse momentum. Baseline leptons (electrons and muons) are also used to apply a second-lepton veto to suppress dilepton $t\bar{t}$ and Wt events. All events must satisfy a series of quality criteria before being considered for further use. The reconstructed primary vertex with the highest $\sum_{\text{tracks}} p_T^2$ must have at least two associated tracks with $p_T > 400$ MeV.

Electron candidates are reconstructed from electromagnetic calorimeter cell clusters that are matched to ID tracks. Baseline electrons are required to have $p_T > 7$ GeV, $|\eta| < 2.47$, and satisfy ‘VeryLoose’ likelihood identification criteria that are defined following the methodology described in Ref. [80]. Signal electrons must pass all baseline requirements and in addition have $p_T > 25$ GeV, satisfy the ‘Loose’ likelihood identification criteria in Ref. [80], and have impact parameters with respect to the reconstructed primary vertex along the beam direction (z_0) and in the transverse plane (d_0) that satisfy $|z_0 \sin \theta| < 0.5$ mm and $|d_0|/\sigma_{d_0} < 5$, where σ_{d_0} is the uncertainty of d_0 . Furthermore, signal electrons must be isolated, where the criteria use track-based information to obtain a 99% efficiency that is independent of p_T , as derived from $Z \rightarrow \ell\ell$ MC samples and confirmed in data [81].

Muons are reconstructed from combined tracks that are formed from ID and MS tracks, ID tracks matched to MS track segments, standalone MS tracks, or ID tracks matched to an energy deposit in the calorimeter compatible with a minimum-ionizing particle (referred to as calo-tagged muon) [82]. Baseline muons are required to have $p_T > 6$ GeV, $|\eta| < 2.6$, and satisfy the ‘Loose’ identification criteria described in Ref. [82]. Signal muons must pass all baseline requirements and in addition have $p_T > 25$ GeV, and have impact parameters $|z_0 \sin \theta| < 0.5$ mm and $|d_0|/\sigma_{d_0} < 3$. Furthermore, signal muons must be isolated according to isolation criteria similar to those used for signal electrons, yielding the same efficiency.

Photon identification is not used in the main event selection, and photons are reconstructed as extra jet or electron candidates. Photons must be identified, however, for the $t\bar{t} + \gamma$ sample that is used in the

⁵ This choice is motivated by the similarity of QCD calculations for the two processes as well as empirical studies of the ratio of K -factors computed as a function of the boson p_T . Further information about the K -factor and its uncertainty is given in Section 7.

data-driven estimation of the $t\bar{t} + Z$ background. In this case, photon candidates are reconstructed from calorimeter cell clusters and are required to satisfy the ‘Tight’ identification criteria described in Ref. [83]. Furthermore, photons are required to have $p_T > 145$ GeV and $|\eta| < 2.37$, excluding the barrel-endcap calorimeter transition in the range $1.37 < |\eta| < 1.52$, so that the photon trigger is fully efficient. Photons must further satisfy ‘Tight’ isolation criteria based on both track and calorimeter information.

Jet candidates are built from topological clusters [84, 85] in the calorimeters using the anti- k_t algorithm with a jet radius parameter $R = 0.4$ [86]. Jets are corrected for contamination from pileup using the jet area method [87–89] and then calibrated to account for the detector response [90, 91]. Jets in data are further calibrated based on *in situ* measurements of the jet energy scale. Baseline jets are required to have $p_T > 20$ GeV. Signal jets must have $p_T > 25$ GeV and $|\eta| < 2.5$. Furthermore, signal jets with $p_T < 60$ GeV are required to satisfy criteria designed to reject jets originating from pileup [89]. Events containing a jet that does not pass specific jet quality requirements are vetoed from the analysis in order to suppress detector noise and non-collision backgrounds [92, 93]. Jets resulting from b -quarks (called b -jets) are identified using the MV2c10 b -tagging algorithm, which is based on quantities such as impact parameters of associated tracks and reconstructed secondary vertices [94, 95]. This algorithm is used at a working point that provides 77% b -tagging efficiency in simulated $t\bar{t}$ events, and corresponds to a rejection factor of about 134 for light-quark flavors and gluons and about 6 for charm jets. Jets and associated tracks are also used to identify hadronically decaying τ leptons using the ‘Loose’ identification criteria described in Refs. [96, 97], which has a 60% and 50% efficiency for reconstructing τ leptons decaying into one and three charged pions, respectively. These τ candidates are required to have one or three associated tracks, with total electric charge opposite to that of the selected electron or muon, $p_T > 20$ GeV, and $|\eta| < 2.5$. This τ candidate p_T requirement is applied after a dedicated energy calibration [97].

The missing transverse momentum is reconstructed from the negative vector sum of the transverse momenta of baseline electrons, muons, jets, and a *soft-term* built from high-quality tracks that are associated with the primary vertex but not with the baseline physics objects [98, 99]. For the event selections requiring photons, the calibrated photon is directly included in the E_T^{miss} calculation. In all other cases, photons and hadronically decaying τ leptons are not explicitly included but enter as jets or electrons, or via the soft-term.

To avoid labeling the same detector signature as more than one object, an overlap removal procedure is applied. The procedure is tailored for this analysis and optimized using simulation. Table 2 summarizes the procedure. Given a set of baseline objects, the procedure checks for overlap based on either a shared track, ghost-matching [88], or a minimal distance ΔR between pairs of objects. For example, if a baseline electron and a baseline jet are found with $\Delta R < 0.2$, then the electron is retained (as stated in the ‘Precedence’ row) and the jet is discarded, unless the jet is b -tagged (as stated in the ‘Condition’ row) in which case the electron is assumed to stem from a heavy-flavor decay and is hence discarded while the jet is retained. If the matching requirement in Table 2 is not met, then both objects under consideration are kept. The order of steps in the procedure is given by the columns in Table 2, which are executed from left to right. The second (ej) and the third (μj) steps of the procedure ensure that leptons and jets have a minimum ΔR separation of 0.2. Therefore, the fourth step (ℓj) only has an effect for $\Delta R > 0.2$. The steps involving a photon are not applied in the main event selection, but only for the event selection where photons are identified. For the remainder of the note, all baseline and signal objects are those that have survived the overlap removal procedure.

Large-radius jets are clustered from all signal (small-radius $R = 0.4$) jets using the anti- k_t algorithm with $R = 1.0$ or 1.2 . To reduce the impact of soft radiation and pileup, the large-radius jets are groomed using reclustered jet trimming, where constituents with p_T less than 5% of the ungroomed jet p_T are

Object 1	e	e	μ	ℓ	γ	γ	τ
Object 2	μ	j	j	j	j	e	e
Matching criteria	shared track	$\Delta R < 0.2$	ghost-matched	$\Delta R < \min\left(0.4, 0.04 + \frac{10}{p_T^\ell/\text{GeV}}\right)$	$\Delta R < 0.2$	$\Delta R < 0.1$	$\Delta R < 0.1$
Condition	calo-tagged μ	j not b -tagged	j not b -tagged and $\left(n_{\text{track}}^j < 3 \text{ or } \frac{p_T^\mu}{p_T^j} > 0.7\right)$		–	–	–
Precedence	e	e	μ	j	γ	e	e

Table 2: Overlap removal procedure. The first two rows list the types of overlapping objects: electrons (e), muons (μ), electron or muon (ℓ), jets (j), photons (γ), and hadronically decaying τ lepton (τ). All objects refer to the baseline definitions, except for γ and τ where no distinction between baseline and signal definition is made. The third row specifies when an object pair is considered as overlapping, the fourth row describes an optional condition, and the last row lists which label is given to the ambiguous object. More information is given in the text.

removed [100–103]. Electrons and muons are not included in the reclustering, since it was found that including them increases the background acceptance more than the signal efficiency. Large-radius jets are not used in the overlap removal procedure; however, the signal jets that enter the reclustering have passed the overlap removal procedure described above. The analysis uses a large-radius jet mass, where the squared mass is defined as the square of the four-vector sum of the constituent (small-radius) jets’ momenta.

All events are required to have $E_T^{\text{miss}} > 200$ GeV, exactly one signal lepton, and no additional baseline leptons. In addition, the transverse mass⁶ of the signal lepton and the missing transverse momentum must satisfy $m_T > 30$ GeV, and the azimuthal angle between leading or sub-leading jet and the missing transverse momentum must be $|\Delta\phi(\text{jet}_i, \vec{p}_T^{\text{miss}})| > 0.4$ with $i \in \{1, 2\}$. The events must further pass an $H_{T,\text{sig}}^{\text{miss}} > 5$ requirement, where $H_{T,\text{sig}}^{\text{miss}} = (H_T^{\text{miss}} - 100 \text{ GeV})/\sigma_{H_T^{\text{miss}}}$. The variable H_T^{miss} is the magnitude of the negative vector sum of the transverse momenta of signal jets and the signal lepton; the resolution $\sigma_{H_T^{\text{miss}}}$ is computed using the per-event jet energy resolution uncertainties (more details are given in Refs. [24, 104]). The latter three event selection criteria suppress multijet processes with misidentified or non-prompt leptons and mismeasured E_T^{miss} to a negligible level. With the above event selection, the dominant backgrounds are $t\bar{t}$ events with at least one leptonically decaying W boson, and W +jets production. A powerful technique for suppressing these background processes is to require m_T to be greater than the W boson mass. For example, an $m_T > 120$ GeV requirement removes more than 90% of the remaining $t\bar{t}$ and W +jets events.

One of the dominant contributions to the residual background is from $t\bar{t}$ production where both W bosons decay leptonically, or one W boson decays leptonically and the other via a hadronic τ decay. A series of additional variables, described in detail in Ref. [24], are used to discriminate between this background and the signal processes. The m_{top}^χ variable is the invariant mass of the three jets in the event most compatible with the hadronic decay products of a top quark, where the three jets are selected by a χ^2 -minimization including the jet momenta and energy resolutions. The asymmetric m_{T2} (am_{T2}) [105–108] and m_{T2}^τ are both variants of the variable m_{T2} [109], a generalization of the transverse mass applied to signatures where two particles are not directly detected. The am_{T2} variable targets dileptonic $t\bar{t}$ events where one lepton is not reconstructed, while the m_{T2}^τ variable targets $t\bar{t}$ events where one of the two W bosons decays via a hadronically decaying τ lepton. Events are removed if one of the selected jets is additionally identified as a hadronic τ candidate, with a corresponding $m_{T2}^\tau < 80$ GeV, where m_{T2}^τ uses the signal lepton and hadronic

⁶ The transverse mass m_T is defined as $m_T^2 = 2p_T^{\text{lep}} E_T^{\text{miss}} [1 - \cos(\Delta\phi)]$, where $\Delta\phi$ is the azimuthal angle between the lepton and the missing transverse momentum direction. The quantity p_T^{lep} is the transverse momentum of the charged lepton.

τ candidate as the two visible objects [19]. The *topness* [110] variable is based on minimizing a χ^2 -type function quantifying the compatibility with a dileptonic $t\bar{t}$ event where one lepton is not reconstructed. The $E_{T,\perp}^{\text{miss}}$ variable is used to further reduce the backgrounds, where E_T^{miss} is aligned with the leptonic top direction. After reconstructing the hadronic top through the χ^2 minimization, the remaining b -jet is paired with the lepton to reconstruct the leptonic top. After boosting the leptonic top and E_T^{miss} into the $t\bar{t}$ rest frame, the perpendicular component of the E_T^{miss} with respect to the leptonic top is computed. This $E_{T,\perp}^{\text{miss}}$ is expected to be smaller for the background due to the dominant contribution of the neutrino in the total E_T^{miss} .

5 Signal Regions

Seven signal event selections (called signal regions, or SR) are constructed using the set of discriminating variables described in Section 4. Six signal regions are newly optimized, before looking at the data, to maximize the discovery sensitivity using benchmark signal models, each representing a distinct phenomenology. Given the small excess observed in one signal region (SR1) in the previous analysis [19], this SR is included without modifications in order to monitor the excess.

Two signal regions (SR1 and `tN_high`) are used to cover the \tilde{t}_1 and $\tilde{\chi}_1^0$ mass plane, under the assumption of 100% \mathcal{BR} to $\tilde{t}_1 \rightarrow t + \tilde{\chi}_1^0$ decay. The SR1 targets the region with low mass splitting between the \tilde{t}_1 and $\tilde{\chi}_1^0$, where the decay products are fully resolved. The `tN_high` targets the region with high mass splitting, leading to very boosted top quarks where the decay products are close-by and can be reconstructed within a single large- R jet. The benchmark points used for the optimization in the $(\tilde{t}_1, \tilde{\chi}_1^0)$ plane are (600, 200) GeV for SR1 and (800, 1) GeV for `tN_high`, respectively.

Two signal regions (`bC2x_diag` and `bC2x_med`) are used to cover the $(\tilde{t}_1, \tilde{\chi}_1^\pm, \tilde{\chi}_1^0)$ mass plane, under the assumption of 100% \mathcal{BR} to $\tilde{t}_1 \rightarrow b + \tilde{\chi}_1^\pm$ decay and $m_{\tilde{\chi}_1^\pm} = 2m_{\tilde{\chi}_1^0}$. The `bC2x_diag` is designed for scenarios where the mass splitting between stop and neutralino is relatively small⁷, while the `bC2x_med` covers the scenarios of large mass splitting. The kinematics of the decay products are governed by the different mass splittings, producing high- p_T b -jets from the $\tilde{t}_1 - \tilde{\chi}_1^\pm$ mass splitting and high- p_T W bosons from the $\tilde{\chi}_1^\pm - \tilde{\chi}_1^0$ splitting. The benchmark points used for the optimization are (600, 500, 250) GeV and (650, 300, 150) GeV respectively.

A fifth signal region (`bCbv`) is designed to target the $(\tilde{t}_1, \tilde{\chi}_1^\pm, \tilde{\chi}_1^0)$ mass plane, under the assumption of 100% \mathcal{BR} to $\tilde{t}_1 \rightarrow b + \tilde{\chi}_1^\pm$ decay and $m_{\tilde{\chi}_1^\pm} = m_{\tilde{t}_1} - 10$ GeV. In this scenario the b -jets from the \tilde{t}_1 decay are too soft to be reconstructed and the sensitivity can be increased by requiring a b -veto in the event. The large mass splitting between chargino and neutralino leads to boosted W bosons. The signal benchmark considered for this SR is (700, 690, 1) GeV.

The last two signal regions (`DM_low` and `DM_high`) are designed to be sensitive to DM production in association with top quarks. The benchmark signals targeted by the two SRs in the $(m_\phi, m_\chi, g_{q,\chi})$ parameter space are (100 GeV, 1 GeV, 1) and (350 GeV, 1 GeV, 3.5), respectively.

The signal region definitions are summarized in Table 3. The signal regions are not mutually exclusive.

⁷ The mass splitting is large enough for b -jets to be reconstructed and identified. For small enough mass splitting the b -jets can become too soft to be reconstructed.

Common event selection			
Trigger	E_T^{miss} trigger		
Lepton	exactly one signal lepton (e, μ), no additional baseline leptons		
Jets	at least two signal jets, and $ \Delta\phi(\text{jet}_i, \vec{p}_T^{\text{miss}}) > 0.4$ for $i \in \{1, 2\}$		
Hadronic τ veto*	veto events with a hadronic τ decay and $m_{T2}^\tau < 80 \text{ GeV}$		
Variable	SR1	tN_high	
Number of (jets, b -tags)	$(\geq 4, \geq 1)$	$(\geq 4, \geq 1)$	
Jet $p_T > [\text{GeV}]$	(80 50 40 40)	(120 80 50 25)	
$E_T^{\text{miss}} [\text{GeV}]$	> 260	> 450	
$E_{T,\perp}^{\text{miss}} [\text{GeV}]$	–	> 180	
$H_{T,\text{sig}}^{\text{miss}}$	> 14	> 22	
$m_T [\text{GeV}]$	> 170	> 210	
$am_{T2} [\text{GeV}]$	> 175	> 175	
$topness$	> 6.5	–	
$m_{\text{top}}^\chi [\text{GeV}]$	< 270	–	
$\Delta R(b, \ell)$	< 3.0	< 2.4	
Leading large-R jet $p_T [\text{GeV}]$	–	> 290	
Leading large-R jet mass $[\text{GeV}]$	–	> 70	
$\Delta\phi(\vec{p}_T^{\text{miss}}, 2^{\text{nd}}\text{large-R jet})$	–	> 0.6	
Variable	bC2x_diag	bC2x_med	bCbv
Number of (jets, b -tags)	$(\geq 4, \geq 2)$	$(\geq 4, \geq 2)$	$(\geq 2, = 0)$
Jet $p_T > [\text{GeV}]$	(70 60 55 25)	(170 110 25 25)	(120 80)
b -tagged jet $p_T > [\text{GeV}]$	(25 25)	(105 100)	–
$E_T^{\text{miss}} [\text{GeV}]$	> 230	> 210	> 360
$H_{T,\text{sig}}^{\text{miss}}$	> 14	> 7	> 16
$m_T [\text{GeV}]$	> 170	> 140	> 200
$am_{T2} [\text{GeV}]$	> 170	> 210	–
$ \Delta\phi(\text{jet}_i, \vec{p}_T^{\text{miss}}) (i = 1)$	> 1.2	> 1.0	> 2.0
$ \Delta\phi(\text{jet}_i, \vec{p}_T^{\text{miss}}) (i = 2)$	> 0.8	> 0.8	> 0.8
Leading large-R jet mass $[\text{GeV}]$	–	–	[70, 100]
$\Delta\phi(\vec{p}_T^{\text{miss}}, \ell)$	–	–	> 1.2
Variable	DM_low	DM_high	
Number of (jets, b -tags)	$(\geq 4, \geq 1)$	$(\geq 4, \geq 1)$	
Jet $p_T > [\text{GeV}]$	(60 60 40 25)	(50 50 50 25)	
$E_T^{\text{miss}} [\text{GeV}]$	> 300	> 330	
$H_{T,\text{sig}}^{\text{miss}}$	> 14	> 9.5	
$m_T [\text{GeV}]$	> 120	> 220	
$am_{T2} [\text{GeV}]$	> 140	> 170	
$\min(\Delta\phi(\vec{p}_T^{\text{miss}}, \text{jet}_i))(i \in \{1 - 4\})$	> 1.4	> 0.8	
$\Delta\phi(\vec{p}_T^{\text{miss}}, \ell)$	> 0.8	–	

Table 3: Overview of the event selections for the seven SRs considered in the analysis. Round brackets are used to describe lists of values and square brackets denote intervals. *The hadronic tau veto is not applied to the bCbv SR, since the $t\bar{t}$ background is negligible.

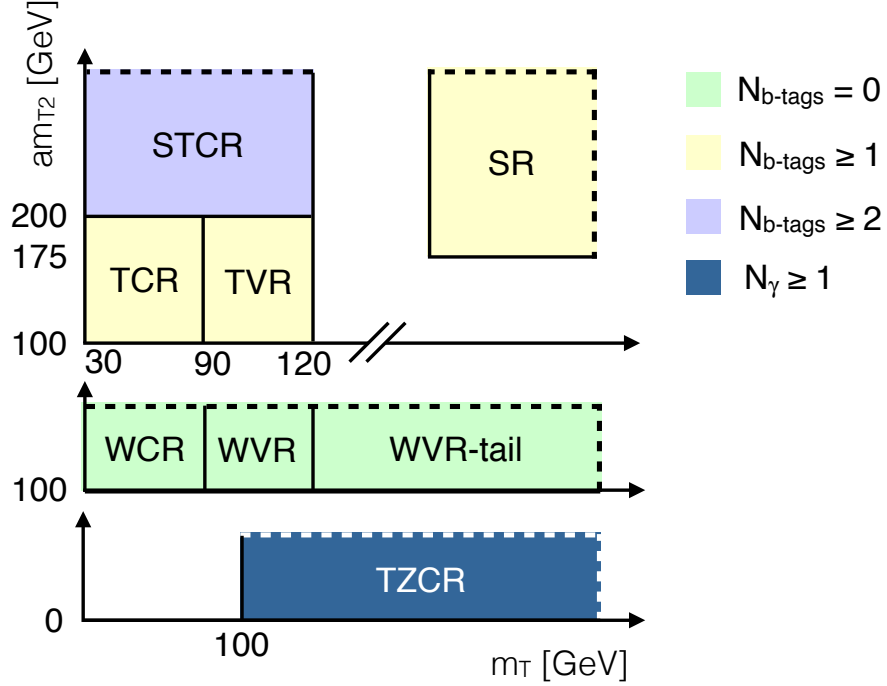


Figure 3: A schematic diagram for the various event selections used to estimate and validate the background normalizations. Solid lines indicate kinematic boundaries while dashed lines indicate that the events can extend beyond the boundary. CR, VR, and SR stand for control region, validation region, and signal region, respectively. T, ST, TZ, and W stand for $t\bar{t}$, single top, $t\bar{t} + Z$, and W +jets, respectively.

6 Background Estimates

The dominant background processes are $t\bar{t}$, single top Wt , $t\bar{t} + Z(\rightarrow \nu\bar{\nu})$, and W +jets. Most of the $t\bar{t}$ and Wt events in the signal regions (SR) have both W bosons decaying leptonically (where one of the two leptons is ‘lost’, meaning it is either not reconstructed, not identified, or removed by the overlap removal procedure) or one W boson decaying leptonically and the other via a hadronically decaying τ lepton. Other background processes considered are dibosons, $t\bar{t} + W$, Z +jets, and multijet events. The combined $t\bar{t} + W$ and $t\bar{t} + Z$ background is referred to as $t\bar{t} + V$.

The main background processes are estimated by isolating each of them in a dedicated control region (CR), described in Section 6.1, normalizing simulation to match data in a simultaneous fit. The fit is performed separately for each SR with the associated CRs. The background modeling as predicted by the fits is tested in a series of validation regions (VR), discussed in Section 6.2. Figure 3 schematically illustrates the setup for one example SR and its associated CRs and VRs.

The contribution of multijet background is estimated and found to be negligible. All other small backgrounds are determined from simulation and normalized to the most accurate theoretical cross-section available.

6.1 Control Regions

A series of CRs are defined as event selections that are kinematically close to the SRs but with a few key variable requirements inverted to significantly reduce signal contamination and enhance the yield and purity of a particular background. These CRs are then used to constrain the background normalization. Each SR has a dedicated CR for each of the following background processes: $t\bar{t}$ (TCR), W +jets (WCR), single top (STCR), and $t\bar{t} + W/Z$ (TZCR), except for bCbb where only TCR and WCR are defined as the contribution of Wt and $t\bar{t} + W/Z$ are found to be negligible after the b -veto requirement. The general strategy in constructing the CRs is to *invert* the transverse mass requirement from a high threshold to a low window. The requirements on several variables are loosened to increase the statistical power of the CR. The details of the TCR and the WCR are described in Section 6.1.1, while the STCR and TZCR are documented in Section 6.1.2 and 6.1.3, respectively. Tables 4 - 6 present an overview of the CR selections for the TCR, WCR, and STCR corresponding to all SRs. The TZCRs have a common selection and only differ on the jet p_T requirements. To obtain a set of background predictions that are independent of the observations in the SRs, a likelihood fit is performed for each SR [111]. The fit can be configured to use only the CRs to constrain the four fit parameters corresponding to the normalizations of $t\bar{t}$, single top, W +jets, and $t\bar{t} + W/Z$ events in the CRs. This fit configuration is referred to as the background-only fit. The E_T^{miss} distribution for the CRs associated with SR1 are shown in Figure 4.

6.1.1 Top and W CRs

The TCRs and WCRs are constructed by modifying the m_T selection in the SRs to be a window whose upper edge is near the W boson mass. An additional upper bound on am_{T2} is applied to the TCRs in order to make them orthogonal to the STCRs, described in the next section. Furthermore, some other kinematic requirements are relaxed or removed to increase the event yields in the CRs. The resulting selections are enriched in semileptonic $t\bar{t}$ events with purities that vary between 51% and 91%. The WCRs are built from the TCRs by changing the b -jet requirement to a b -jet veto, and the am_{T2} requirement is relaxed where needed to improve the statistics of the WCR. The b -jet veto suppresses $t\bar{t}$ events and results in a W +jets purity of approximately 75% in the WCRs.

6.1.2 Single Top CRs

All of the expected single-top contributions in the SRs are from the Wt process. This process can evade kinematic bounds from selections targeting the suppression of $t\bar{t}$. Nonetheless, isolating a pure sample of Wt events kinematically close to the SRs is challenging due to the similarity of the Wt and $t\bar{t}$ processes. The Wt events that pass event selections similar to those for the SRs often have a second b -jet within the acceptance. The am_{T2} variable is useful for discriminating Wt events from $t\bar{t}$ events because the mass of the Wb system not from the resonant top quark is typically higher than for an on-shell top quark in the phase space selected by this analysis. Therefore, the STCRs all require $am_{T2} > 200$ GeV. Furthermore, to increase the purity of Wt and reduce the W +jets contamination, events are required to have two b -tagged jets.

The $t\bar{t}$ events can exceed the am_{T2} kinematic bound when one of the two b -tags used in the am_{T2} calculation is a charm quark from the W decay misidentified as a b -tagged jet. When the mistagged jet is from the same top quark as the other b -tagged jet, the ΔR between the two b -tags tends to be smaller than for the Wt events that have two b -jets from b -quarks. Therefore, to further increase the Wt purity, events in the

Common event selection for tN			
Trigger	E_T^{miss} trigger		
Lepton	exactly one signal lepton (e, μ), no additional baseline leptons		
Jets	at least four signal jets, and $ \Delta\phi(\text{jet}_i, \vec{p}_T^{\text{miss}}) > 0.4$ for $i \in \{1, 2\}$		
Hadronic τ veto	veto events with a hadronic τ decay and $m_{T2}^\tau < 80$ GeV		
Variable	SR1	TCR / WCR	STCR
≥ 4 jets with $p_T > [\text{GeV}]$	(80 50 40 40)	(80 50 40 40)	(80 50 40 40)
E_T^{miss} [GeV]	> 260	> 200	> 200
$H_{T,\text{sig}}^{\text{miss}}$	> 14	> 5	> 5
m_T [GeV]	> 170	[30,90]	[30,120]
am_{T2} [GeV]	> 175	[100,200] / > 100	> 200
$topness$	> 6.5	> 6.5	> 6.5
m_{top}^χ [GeV]	< 270	< 270	< 270
$\Delta R(b, \ell)$	< 3.0	–	–
$\Delta R(b_1, b_2)$	–	–	> 1.2
Number of b -tags	≥ 1	≥ 1 / $= 0$	≥ 2
Variable	tN_high	TCR / WCR	STCR
≥ 4 jets with $p_T > [\text{GeV}]$	(120 80 50 25)	(120 80 50 25)	(120 80 50 25)
E_T^{miss} [GeV]	> 450	> 300	> 250
$E_{T,\perp}^{\text{miss}}$ [GeV]	> 180	> 160	> 160
$H_{T,\text{sig}}^{\text{miss}}$	> 22	> 15	> 10
m_T [GeV]	> 210	[30,90]	[30,120]
am_{T2} [GeV]	> 175	[100,200] / > 100	> 200
$\Delta R(b, \ell)$	< 2.4	–	–
$\Delta R(b_1, b_2)$	–	–	> 1.2
Number of b -tags	≥ 1	≥ 1 / $= 0$	≥ 2
Leading large-R jet p_T [GeV]	> 290	> 290	> 290
Leading large-R jet mass [GeV]	> 70	> 70	> 70
$\Delta\phi(\vec{p}_T^{\text{miss}}, 2^{\text{nd}} \text{large-R jet})$	> 0.6	> 0.6	> 0.6

Table 4: Overview of the event selections for tN SRs and the associated $t\bar{t}$ (TCR), W +jets (WCR), and Wt (STCR) control regions. Round brackets are used to describe lists of values and square brackets denote intervals.

Common event selection for bC			
Trigger	E_T^{miss} trigger		
Lepton	exactly one signal lepton (e, μ), no additional baseline leptons		
Jets	at least two signal jets, and $ \Delta\phi(\text{jet}_i, \vec{p}_T^{\text{miss}}) > 0.4$ for $i \in \{1, 2\}$		
Hadronic τ veto*	veto events with a hadronic τ decay and $m_{T2}^\tau < 80$ GeV		
Variable	bC2x_diag	TCR / WCR	STCR
≥ 4 jets with $p_T > [\text{GeV}]$	(70 60 55 25)	(70 60 55 25)	(70 60 55 25)
≥ 2 b -tagged jets with $p_T > [\text{GeV}]$	(25 25)	(25 25) / –	(25 25)
E_T^{miss} [GeV]	> 230	> 230	> 230
$H_{T,\text{sig}}^{\text{miss}}$	> 14	> 14	> 5
m_T [GeV]	> 170	[30,90]	[30,120]
am_{T2} [GeV]	> 170	[100, 200] / > 170	> 200
$ \Delta\phi(\text{jet}_i, \vec{p}_T^{\text{miss}}) (i = 1)$	> 1.2	> 1.2	> 1.2
$ \Delta\phi(\text{jet}_i, \vec{p}_T^{\text{miss}}) (i = 2)$	> 0.8	> 0.8	> 0.8
$\Delta R(b_1, b_2)$	–	–	> 1.4
Number of b -tags	≥ 2	$\geq 2 / = 0$	≥ 2
Variable	bC2x_med	TCR / WCR	STCR
≥ 4 jets with $p_T > [\text{GeV}]$	(170 110 25 25)	(170 110 25 25)	(170 110 25 25)
≥ 2 b -tagged jets with $p_T > [\text{GeV}]$	(105 100)	(105 100) / –	(105 100)
E_T^{miss} [GeV]	> 210	> 210	> 210
$H_{T,\text{sig}}^{\text{miss}}$	> 7	> 7	> 7
m_T [GeV]	> 140	[30,90]	[30,120]
am_{T2} [GeV]	> 210	[100, 210] / > 210	> 210
$ \Delta\phi(\text{jet}_i, \vec{p}_T^{\text{miss}}) (i = 1)$	> 1.0	> 1.0	> 1.0
$ \Delta\phi(\text{jet}_i, \vec{p}_T^{\text{miss}}) (i = 2)$	> 0.8	> 0.8	> 0.8
$\Delta R(b_1, b_2)$	–	–	> 1.2
Number of b -tags	≥ 2	$\geq 2 / = 0$	≥ 2
Variable	bCbv	TCR	WCR
≥ 2 jets with $p_T > [\text{GeV}]$	(120 80)	(120 80)	(120 80)
E_T^{miss} [GeV]	> 360	> 360	> 360
$H_{T,\text{sig}}^{\text{miss}}$	> 16	> 16	> 16
m_T [GeV]	> 200	[30,90]	[30,90]
Lepton p_T [GeV]	> 60	> 60	> 60
$ \Delta\phi(\text{jet}_i, \vec{p}_T^{\text{miss}}) (i = 1)$	> 2.0	> 2.0	> 2.0
$ \Delta\phi(\text{jet}_i, \vec{p}_T^{\text{miss}}) (i = 2)$	> 0.8	> 0.8	> 0.8
Number of b -tags	$= 0$	≥ 1	$= 0$
Leading large- R jet mass [GeV]	[70, 100]	[70, 100]	[70, 100]
$\Delta\phi(\vec{p}_T^{\text{miss}}, \ell)$	> 1.2	–	–

Table 5: Overview of the event selections for bC SRs and the associated $t\bar{t}$ (TCR), W +jets (WCR), and Wt (STCR) control regions. Round brackets are used to describe lists of values and square brackets denote intervals. The hadronic tau veto is not applied to the bCbv SR, since the $t\bar{t}$ background is negligible.

Common event selection for DM			
Trigger	E_T^{miss} trigger		
Lepton	exactly one signal lepton (e, μ), no additional baseline leptons		
Jets	at least four signal jets, and $ \Delta\phi(\text{jet}_i, \vec{p}_T^{\text{miss}}) > 0.4$ for $i \in \{1, 2\}$		
Hadronic τ veto	veto events with a hadronic τ decay and $m_{T2}^\tau < 80 \text{ GeV}$		
Variable	DM_low	TCR / WCR	STCR
≥ 4 jets with $p_T > [\text{GeV}]$	(60 60 40 25)	(60 60 40 25)	(60 60 40 25)
E_T^{miss} [GeV]	> 300	$> 200 / > 230$	> 200
$H_{T,\text{sig}}^{\text{miss}}$	> 14	> 8	> 8
m_T [GeV]	> 120	[30,90]	[30,120]
am_{T2} [GeV]	> 140	[100, 200] / > 100	> 200
$\min(\Delta\phi(\vec{p}_T^{\text{miss}}, \text{jet}_i))(i \in \{1 - 4\})$	> 1.4	> 1.4	> 1.4
$\Delta\phi(\vec{p}_T^{\text{miss}}, \ell)$	> 0.8	> 0.8	–
$\Delta R(b_1, b_2)$	–	–	> 1.8
Number of b -tags	≥ 1	$\geq 1 / = 0$	≥ 2
Variable	DM_high	TCR / WCR	STCR
≥ 4 jets with $p_T > [\text{GeV}]$	(50 50 50 25)	(50 50 50 25)	(50 50 50 25)
E_T^{miss} [GeV]	> 330	$> 300 / > 330$	> 250
$H_{T,\text{sig}}^{\text{miss}}$	> 9.5	> 9.5	> 5
m_T [GeV]	> 220	[30,90]	[30,120]
am_{T2} [GeV]	> 170	[100, 200] / > 100	> 200
$\min(\Delta\phi(\vec{p}_T^{\text{miss}}, \text{jet}_i))(i \in \{1 - 4\})$	> 0.8	> 0.8	> 0.8
$\Delta R(b_1, b_2)$	–	–	> 1.2
Number of b -tags	≥ 1	$\geq 1 / = 0$	≥ 2

Table 6: Overview of the event selections for DM SRs and the associated $t\bar{t}$ (TCR), W +jets (WCR), and Wt (STCR) control regions. Round brackets are used to describe lists of values and square brackets denote intervals.

STCRs are required to have $\Delta R(b_1, b_2) > 1.2$ where b_1 and b_2 are the two highest- p_T b -tagged jets. For DM_low and bC2x_diag STCRs, the requirement of the $\Delta R(b_1, b_2)$ is even tighter to increase the purity of Wt events as shown in Tables 5 and 6. The expected purity for Wt events varies between 40 and 50% in the STCRs.

6.1.3 $t\bar{t} + Z$ CRs

Top quark pair production in association with a Z boson that decays into neutrinos is an irreducible background. The expected contributions of $t\bar{t} + W$ in the seven SRs are less than 10% with respect to the expected $t\bar{t} + Z$ yields, and the two processes are combined in the analysis. A CR using Z boson decays to charged leptons is not feasible given the small branching ratio to leptons and the limited dataset available. However, a data-driven approach is still possible using a similar process: $t\bar{t} + \gamma$. The CR is designed to minimize the differences between the two processes, in order to reduce the theoretical uncertainties in the extrapolation. The main differences arise from the Z boson mass, which reduces the available phase space, causing differences in kinematic distributions. In addition, the bremsstrahlung rate for Z

bosons is highly suppressed at LHC energies, while there is a large contribution to the $t\bar{t} + \gamma$ cross-section from photons radiated from the top quark or its decay products. Both of these differences are mitigated if the boson p_T is larger than the Z boson mass. In this limit, the impact of the mass difference on the available phase space is reduced and the rate of photon radiation from bremsstrahlung is suppressed [76]. The small contribution of photon radiations is fully accounted for in the simulation and any uncertainty in their modeling is subdominant compared to the uncertainties described in Section 7. In high- E_T^{miss} $t\bar{t} + Z(\rightarrow \nu\bar{\nu})$ events, the Z boson p_T is the dominant source of E_T^{miss} . Hence most of $t\bar{t} + Z$ events in the SRs have large Z boson p_T .

The event selection for the different TZCRs requires at least one signal photon, exactly one signal lepton and no additional baseline leptons, and at least four signal jets, of which at least one must be b -tagged. Furthermore the TZCRs are required to have the same jet p_T thresholds as the corresponding SRs. To mimic the $Z \rightarrow \nu\bar{\nu}$ decay, the highest- p_T photon is vectorially added to \vec{p}_T^{miss} and this sum is used to construct $\tilde{E}_T^{\text{miss}} = |\vec{p}_T^{\text{miss}} + \vec{p}_T^\gamma|$, \tilde{m}_T , and $\tilde{H}_{T,\text{sig}}^{\text{miss}}$. Events entering the TZCRs are required to satisfy $\tilde{E}_T^{\text{miss}} > 120$ GeV, $\tilde{m}_T > 100$ GeV, and $\tilde{H}_{T,\text{sig}}^{\text{miss}} > 5$ in order to bring the region kinematically closer to the SRs. Finally, $E_T^{\text{miss}} < 200$ GeV is imposed to ensure orthogonality between the TZCR and the other CRs and SRs. The resulting regions have over 90% $t\bar{t} + \gamma$ purity, with the main background being $W + \gamma + \text{jets}$. Without scaling, the total number of events in data is about 30-47% higher than in simulation, but there is no significant evidence of mismodeling of the shapes of the various distributions within uncertainties.

6.2 Validation Regions

The background estimates are tested using VRs, which are disjoint from both the CRs and SRs. Background normalizations determined in the CRs are extrapolated to the VRs and compared with the observed data. Each SR has associated VRs for the $t\bar{t}$ (TVR) and $W + \text{jets}$ (WVR) processes, and these are constructed with the same selection as the TCR/WCR except that m_T is between 90 and 120 GeV.⁸ The VRs are not used to constrain parameters in the fit, but provide a statistically independent test of the background estimates made using the CRs. The potential signal contamination in the VRs is studied for all considered signal models and mass ranges, and found to be negligible.

A second set of VRs, not associated with any of the SRs, is used for further study of the main backgrounds. Two of the more significant backgrounds are dileptonic $t\bar{t}$ and lepton+hadronic $\tau t\bar{t}$ events. The modeling of these backgrounds is validated in dedicated VRs that require either two signal leptons (electron or muon) or one signal lepton and one hadronic τ candidate. In Figure 5 the m_T and am_{T2} distributions are shown for event selections requiring four jets, an electron-muon pair (left) and one lepton plus one τ candidate (right), respectively. The m_T is constructed using the leading lepton. Additional VRs are constructed by considering (1) events with high E_T^{miss} , high m_T , and low am_{T2} for dilepton $t\bar{t}$ events with a lost lepton or (2) high m_T and a b -jet veto to probe the modeling of the resolution-induced m_T tail in $W + \text{jets}$ events (denoted WVR-tail region in Figure 3). There are no significant indications of mismodeling in any of the VRs.

⁸ A Wt VR is not defined since the m_T range in the STCR is extended upward to 120 GeV to accept more events.

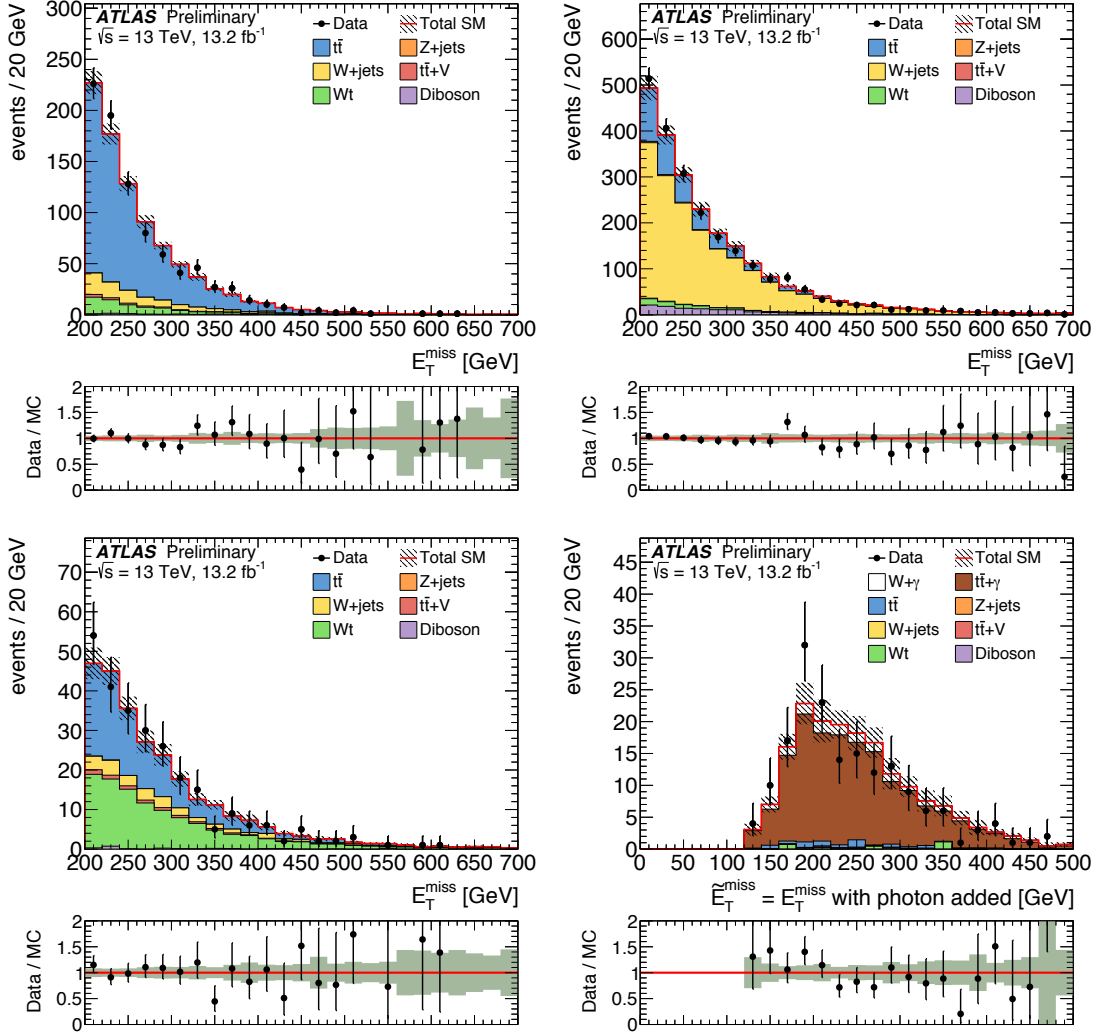


Figure 4: Distributions of E_T^{miss} (top left for TCR, top right for WCR and bottom left for STCR), and photon-corrected E_T^{miss} (bottom right for TZCR) for events in the CRs associated with SR1 where each background ($t\bar{t}$, W +jets, Wt , and $t\bar{t} + W/Z$) is normalized by normalization factors obtained by background-only fits. The uncertainty band includes statistical and all experimental systematic uncertainties. The last bin includes overflow.

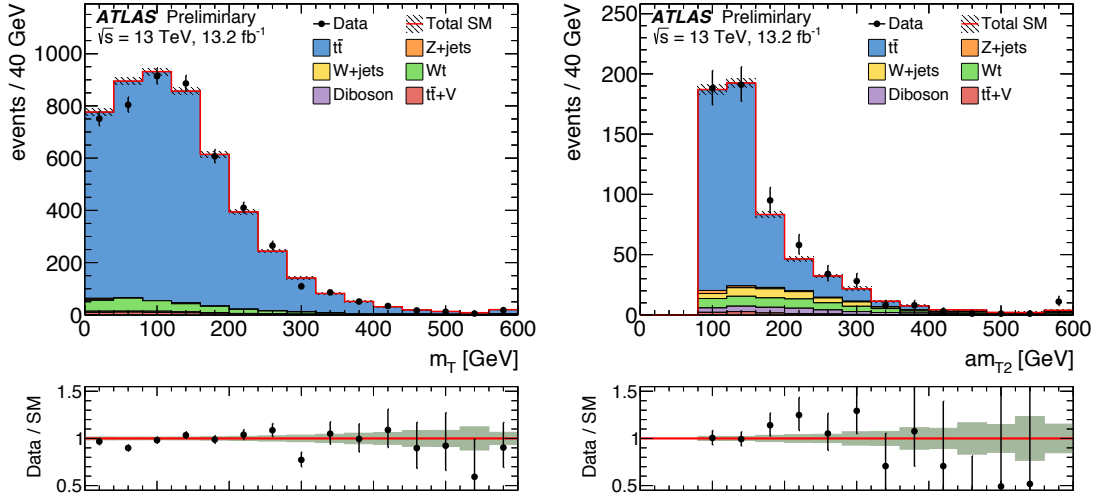


Figure 5: Distributions of m_T and am_{T2} for events with at least four jets and exactly two signal leptons (left) or one lepton plus one τ candidate (right). Backgrounds are normalized to their respective cross sections and no correction factors are applied to the background normalizations. The uncertainty band includes statistical uncertainties. The last bin includes overflow.

7 Systematic Uncertainties

The systematic uncertainties in the signal and background estimates arise both from experimental sources and from the uncertainties in the theoretical predictions and modeling. Since the yields from the dominant background sources, $t\bar{t}$, single top, $t\bar{t}V$, and W +jets, are all obtained in dedicated control regions, the modeling uncertainties for these processes affect only the extrapolation from the CRs into the signal regions (and between the various control regions), but not the overall normalization. The systematic uncertainties are included as nuisance parameters with Gaussian constraints and profiled in the likelihood fits.

The dominant experimental uncertainties arise from imperfect knowledge of the jet energy scale (JES) and jet energy resolution (JER) [91], the modeling of the b -tagging efficiencies for b , c and light-flavor jets [112, 113] as well as the contribution of the E_T^{miss} soft-term, which is composed of tracks neither associated with any reconstructed objects nor identified as originating from pileup. From these sources, the resulting uncertainties in the extrapolation factors for going from the four CRs to the SRs are 4–15% for JES, 0–9% for JER, 0–6% for b -tagging, and 0–3% for the E_T^{miss} soft-term. Other sources of experimental uncertainty are the modeling of lepton- and photon-related quantities (energy scales, resolutions, reconstruction and identification efficiencies, isolation, hadronic- τ identification) and the uncertainty in the integrated luminosity. These uncertainties have a small impact on the final results.

The uncertainties in the modeling of the single-top and $t\bar{t}$ backgrounds include effects related to the MC event generator, the hadronization and fragmentation modeling, and the amount of initial- and final-state radiation [61]. The MC generator uncertainty is estimated by comparing events produced with POWHEG-Box+Herwig++ and with MG5_AMC@NLO+Herwig++. Events generated with POWHEG-Box are hadronized with either PYTHIA or Herwig++ to estimate the effect from the modeling of the fragmentation and hadronization. The impact of altering the amount of initial- and final-state radiation is estimated from comparisons of POWHEG-Box+PYTHIA samples with different parton shower radiation,

NLO radiation, and modified factorization and renormalization scales. One additional uncertainty stems from the modeling of the interference between the $t\bar{t}$ and Wt processes at NLO. The uncertainty is estimated using inclusive $WWbb$ events, generated using MG5_AMC@NLO, which are compared with the sum of the $t\bar{t}$ and Wt processes [61]. The resulting theoretical uncertainties in the extrapolation factors for going from the $t\bar{t}$ and Wt CRs to the SRs are 17–32% for $t\bar{t}$, and 14–68% for Wt events, where the latter is dominated by the interference term.

The $t\bar{t} + Z$ background is normalized using the $t\bar{t} + \gamma$ CR and therefore there are uncertainties in both the kinematic extrapolation to the SR and in the conversion between the two processes. As described in Section 3, a small correction factor (4%) is applied to the $t\bar{t} + \gamma$ cross-section to account for differences in the generator setup, and the same K -factor is used for both processes. A first source of uncertainty is estimated by coherently varying the factorization and renormalization scales between $t\bar{t} + Z$ and $t\bar{t} + \gamma$ events generated at LO by a factor of two. The impact of the scale choice is slightly different between $t\bar{t} + Z$ and $t\bar{t} + \gamma$, leading to a 10% uncertainty for high- p_T bosons. An uncertainty due to NLO corrections is estimated by studying the kinematic dependence of the ratio of $t\bar{t} + Z$ and $t\bar{t} + \gamma$ K -factors. This ratio is studied by computing the K -factor for the $t\bar{t} + Z$ and $t\bar{t} + \gamma$ processes using MG5_AMC@NLO and SHERPA +OpenLoops as a function of the boson p_T , comparing the nominal generator setup with a series of variations. Coherently varying the factorization and renormalization scale (set to $H_T = \sum p_T$ for both LO and NLO) by a factor of two results in a 5% uncertainty in the K -factor ratio. Comparing the results obtained with the NNPDF and the CT14 [114] PDF sets changes the K -factor ratio by less than 2%. An additional uncertainty of 5% is due to the difference in K -factor ratios between the two generators when the same scale and PDF set is used, resulting from a different choice of electroweak scheme. The resulting theoretical systematic uncertainty in the extrapolation from the $t\bar{t} + \gamma$ CR to the SR is 12%.

The uncertainty on the W +jets background is estimated by comparing with MG5_AMC@NLO to account for the MC event generator modeling. The difference is taken as uncertainty, amounting to 10-20%. In addition, the effects of varying the scales for the matching scheme related to the merging of matrix elements and parton showers, renormalization, factorization, and resummation are estimated and are found to be 0-10%. Since the W +jets background is normalized in a CR with a b -tagged jet veto, additional uncertainties in the flavor composition of the W +jets events in the signal region are applied in all regions requiring at least one b -tagged jet. These uncertainties are based on the measurement reported in Ref. [115] extrapolated to higher jet multiplicities. The resulting theoretical uncertainties in the extrapolation from the W +jets CR to the SR amount to about 20% for bC**b**v and 40% for the other SRs.

Since the diboson backgrounds are not normalized in a CR, the analysis is sensitive to the uncertainty in the total cross-section, estimated to be 6%. In addition, the effects of varying the renormalization, factorization, and resummation scales are estimated. The resulting theoretical uncertainties for the diboson yields in the SRs are 20-30%.

The SUSY signal cross-section uncertainty is taken from an envelope of cross-section predictions using different PDF sets and factorization and renormalization scales, as described in Ref. [116], and the resulting uncertainties range from 13% to 23%. The uncertainty on the DM production cross-section is estimated by varying its scale on acceptance, which is found to be 5%.

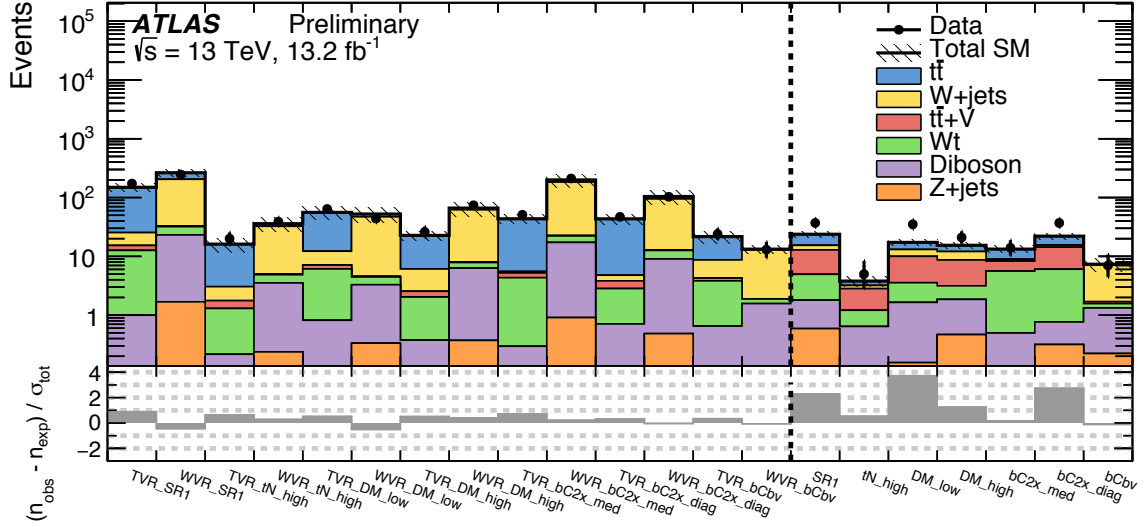


Figure 6: Comparison of the observed data (n_{obs}) with the predicted background (n_{exp}) in the VR and SRs. The background predictions are obtained using the background-only fit configuration. The bottom panel shows the significance of the difference between data and predicted background, where the significance is based on the total uncertainty (σ_{tot}).

8 Results

The number of observed events together with the predicted number of background events in all the SRs is shown in Table 7 and Fig. 6 together with the VRs. The VRs are not mutually exclusive among themselves; the same applies to the SRs. The prediction is obtained using the background-only fit configuration described in Section 6. Table 7 also lists the results for the four fit parameters that control the normalization of the four main backgrounds (normalization factors, NFs), together with the associated fit uncertainties. To quantify the compatibility of the SM background-only hypothesis with the observations in the SRs, a profile likelihood ratio test is performed. All limits are calculated using the CL_s prescription [117]. Table 7 reports the resulting p -values (p_0). The largest deviation from the background prediction is found in DM_low with a local significance of 3.3σ . Mild excesses corresponding to 2.2σ and 2.6σ are also observed in SR1 and bC2x_diag, respectively. A partial overlap exists between the observed data events in the three SRs. It is found that the data excess in SR1 is reduced when considering only the subset of events that are unique to SR1 whereas this is not the case for DM_low and bC2x_diag. Further cross checks were performed to ensure the accuracy of the background estimates and no indications of mismodelings were found.

Figures 7 – 10 show the E_T^{miss} and m_T distributions in four representative SRs.

Exclusion limits are derived in the context of stop pair production models and simplified models for dark matter associated production with top quarks. The signal uncertainties and potential signal contributions to all regions are taken into account. All uncertainties except those on the theoretical signal cross-section are included in the fit. Exclusion limits at 95% CL are obtained by selecting a priori the signal region with the lowest expected CL_s value for each signal model and the exclusion contours are derived by interpolating in the CL_s value.

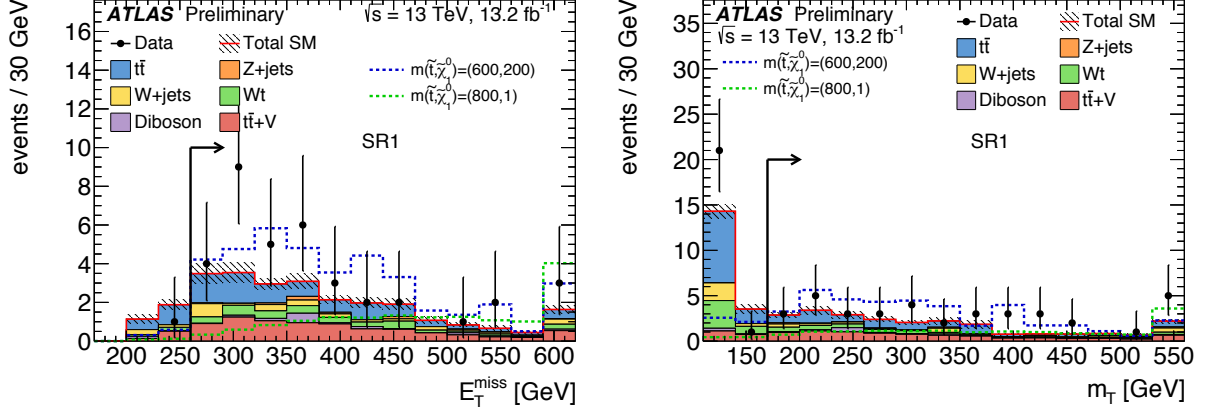


Figure 7: The E_T^{miss} (left) and m_T (right) distributions in SR1. In each plot, the full event selection in the corresponding signal region is applied, except for the requirement (indicated by an arrow) that is imposed on the variable being plotted. The predicted backgrounds are scaled with the NFs documented in Table 7. The uncertainty band includes statistical uncertainties. The last bin contains the overflow. Benchmark signal models are overlaid for comparison.

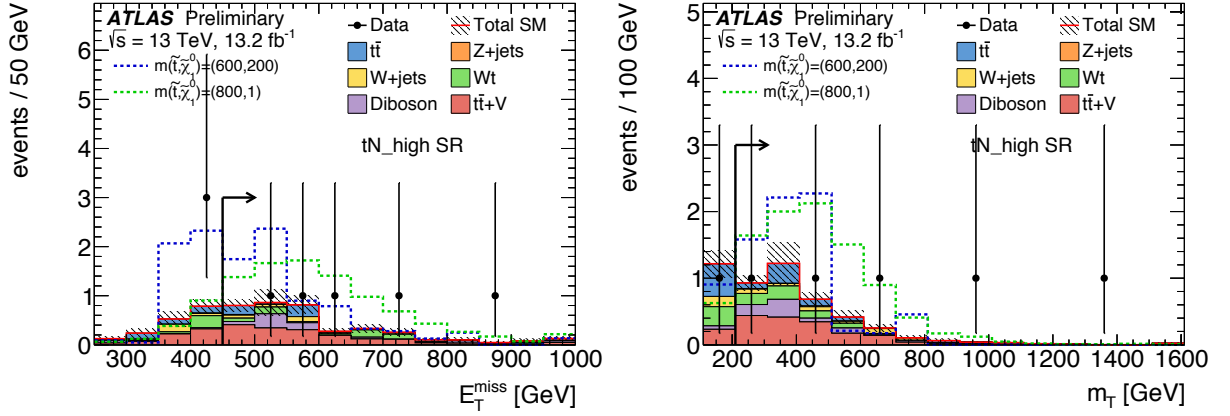


Figure 8: The E_T^{miss} (left) and m_T (right) distributions in tN_high. In each plot, the full event selection in the corresponding signal region is applied, except for the requirement (indicated by an arrow) that is imposed on the variable being plotted. The predicted backgrounds are scaled with the NFs documented in Table 7. The uncertainty band includes statistical uncertainties. The last bin contains the overflow. Benchmark signal models are overlaid for comparison.

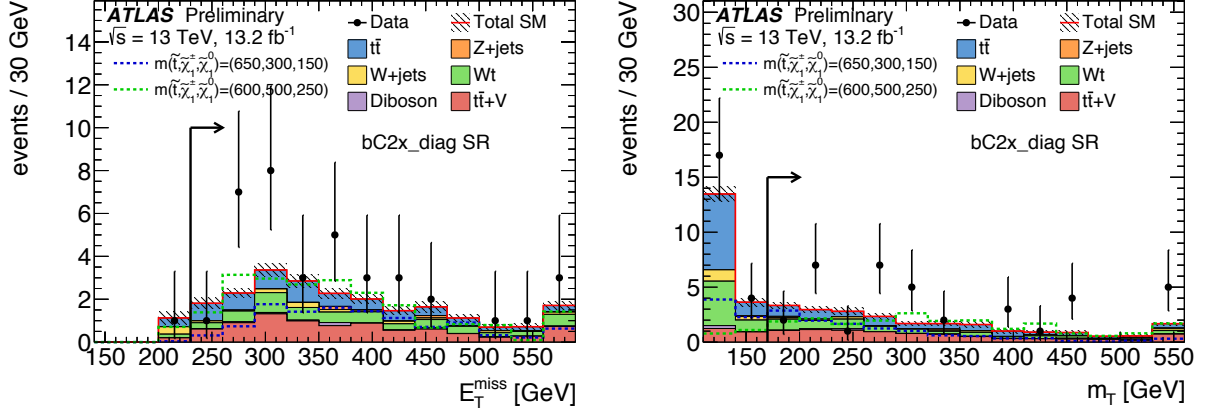


Figure 9: The E_T^{miss} (left) and m_T (right) distributions in bC2x_diag. In each plot, the full event selection in the corresponding signal region is applied, except for the requirement (indicated by an arrow) that is imposed on the variable being plotted. The predicted backgrounds are scaled with the NFs documented in Table 7. The uncertainty band includes statistical uncertainties. The last bin contains the overflow. Benchmark signal models are overlaid for comparison.

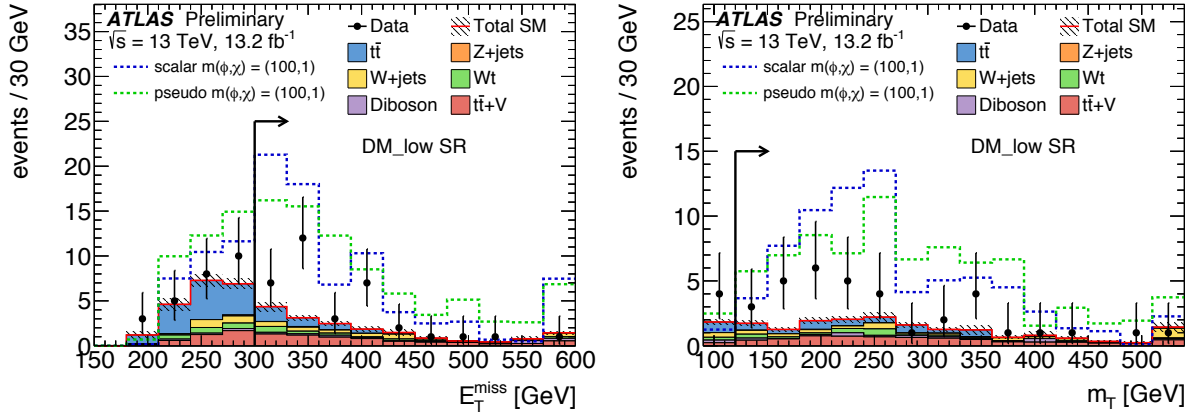


Figure 10: The E_T^{miss} (left) and m_T (right) distributions in DM_low. In each plot, the full event selection in the corresponding signal region is applied, except for the requirement (indicated by an arrow) that is imposed on the variable being plotted. The predicted backgrounds are scaled with the NFs documented in Table 7. The uncertainty band includes statistical uncertainties. The last bin contains the overflow. Benchmark signal models where a common coupling $g = g_q = g_\chi = 3.5$ is assumed are overlaid for comparison.

Signal region	SR1	tN_high	bC2x_diag	bC2x_med	bCbv	DM_low	DM_high
Observed	37	5	37	14	7	35	21
Total background	24 ± 3	3.8 ± 0.8	22 ± 3	13 ± 2	7.4 ± 1.8	17 ± 2	15 ± 2
$t\bar{t}$	8.4 ± 1.9	0.60 ± 0.27	6.5 ± 1.5	4.3 ± 1.0	0.26 ± 0.18	4.2 ± 1.3	3.3 ± 0.8
W +jets	2.5 ± 1.1	0.15 ± 0.38	1.2 ± 0.5	0.63 ± 0.29	5.4 ± 1.8	3.1 ± 1.5	3.4 ± 1.4
Single top	3.1 ± 1.5	0.57 ± 0.44	5.3 ± 1.8	5.1 ± 1.6	0.24 ± 0.23	1.9 ± 0.9	1.3 ± 0.8
$t\bar{t} + V$	7.9 ± 1.6	1.6 ± 0.4	8.3 ± 1.7	2.7 ± 0.7	0.12 ± 0.03	6.4 ± 1.4	5.5 ± 1.1
Diboson	1.2 ± 0.4	0.61 ± 0.26	0.45 ± 0.17	0.42 ± 0.20	1.1 ± 0.4	1.5 ± 0.6	1.4 ± 0.5
Z +jets	0.59 ± 0.54	0.03 ± 0.03	0.32 ± 0.29	0.08 ± 0.08	0.22 ± 0.20	0.16 ± 0.14	0.47 ± 0.44
$t\bar{t}$ NF	1.03 ± 0.07	1.06 ± 0.15	0.89 ± 0.10	0.95 ± 0.12	0.73 ± 0.22	0.90 ± 0.17	1.01 ± 0.13
W +jets NF	0.76 ± 0.08	0.78 ± 0.08	0.87 ± 0.07	0.85 ± 0.06	0.97 ± 0.12	0.94 ± 0.13	0.91 ± 0.07
Single top NF	1.07 ± 0.30	1.30 ± 0.45	1.26 ± 0.31	0.97 ± 0.28	–	1.36 ± 0.36	1.02 ± 0.32
$t\bar{t} + W/Z$ NF	1.43 ± 0.21	1.39 ± 0.22	1.40 ± 0.21	1.30 ± 0.23	–	1.47 ± 0.22	1.42 ± 0.21
p_0 (σ)	0.012 (2.2)	0.26 (0.6)	0.004 (2.6)	0.40 (0.3)	0.50 (0)	0.0004 (3.3)	0.09 (1.3)
$N_{\text{non-SM}}^{\text{limit exp. (95\% CL)}}$	$12.9^{+5.5}_{-3.8}$	$5.5^{+2.8}_{-1.1}$	$12.4^{+5.4}_{-3.7}$	$9.0^{+4.2}_{-2.7}$	$7.3^{+3.5}_{-2.2}$	$11.5^{+5.0}_{-3.4}$	$9.9^{+4.6}_{-2.9}$
$N_{\text{non-SM}}^{\text{limit obs. (95\% CL)}}$	26.0	7.2	27.5	9.9	7.2	28.3	15.6

Table 7: The numbers of observed events in the three SRs together with the expected numbers of background events and their uncertainties as predicted by the background-only fits, the scaling factors for the background predictions in the fit (NF), and the probabilities (represented by the p_0 values) that the observed numbers of events are compatible with the background-only hypothesis.

Figure 11 and 12 show the expected and observed exclusion contours for both decay modes of direct pair production of stops decaying in top plus neutralino ($t\tilde{\chi}_1^0$) and in b plus chargino ($b\tilde{\chi}_1^\pm$) final states. The $\pm 1\sigma_{\text{exp}}$ (yellow) uncertainty band indicates the impact on the expected limit of all uncertainties included in the fit. For the direct stop pair production models the results extend previous exclusion limits by excluding the stop mass region up to 830 GeV for a massless lightest neutralino under the assumption of $\mathcal{BR}(\tilde{t}_1 \rightarrow t + \tilde{\chi}_1^0) = 100\%$. Exclusion limits are also extended in stop pair production models with $\mathcal{BR}(\tilde{t}_1 \rightarrow b + \tilde{\chi}_1^\pm) = 100\%$ under different hypotheses of the mass splitting. Considering $m_{\tilde{\chi}_1^\pm} = 2m_{\tilde{\chi}_1^0}$, stops with a mass of 750 GeV are excluded for a 150 GeV neutralino mass. Stop masses up to 750 GeV for a massless lightest neutralino are also excluded under the assumption of $m_{\tilde{\chi}_1^\pm} = m_{\tilde{t}_1} - 10$ GeV. Previous exclusion limits are obtained under the hypothesis of mostly right-handed (left-handed) stops in the case of $\tilde{t}_1 \rightarrow t + \tilde{\chi}_1^0$ ($\tilde{t}_1 \rightarrow b + \tilde{\chi}_1^\pm$) decays. The assumption of unpolarized stops yields slightly weaker limits in both planes than the corresponding polarized assumption. Limits are also placed in scenarios where both the $\tilde{t}_1 \rightarrow t + \tilde{\chi}_1^0$ and $\tilde{t}_1 \rightarrow b + \tilde{\chi}_1^\pm$ decay modes are allowed under the assumption of $m_{\tilde{\chi}_1^\pm} = 2m_{\tilde{\chi}_1^0}$. Five different \mathcal{BR} assumptions are tested with 0, 25, 50, 75 and 100 % \mathcal{BR} to $\tilde{t}_1 \rightarrow t + \tilde{\chi}_1^0$. The results are shown in Figure 13.

Results for simplified dark matter models are also obtained. Figure 14 shows the values of the common coupling, $g = g_q = g_\chi$, that are excluded for dark matter associated production with top quarks under the assumption of a scalar or pseudo-scalar mediator. The maximal coupling of $g = g_q = g_\chi = 3.5$ is excluded at 95% confidence level in a wide range of mediator masses, up to 350 GeV for a 1 GeV dark matter particle mass.

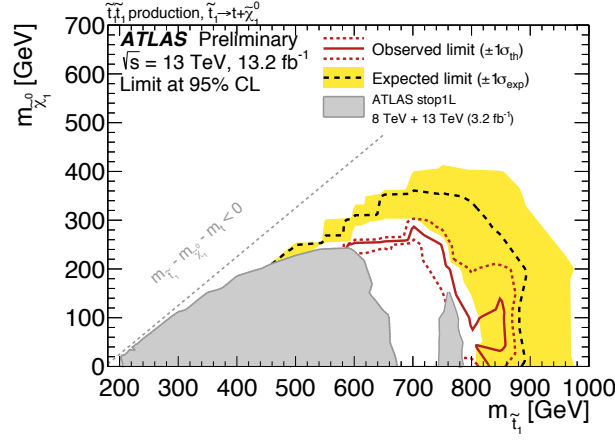


Figure 11: Expected (black dashed) and observed (red solid) 95% excluded regions in the plane of $m_{\tilde{t}_1}$ versus $m_{\tilde{\chi}_1^0}$ for direct stop pair production assuming $t\tilde{\chi}_1^0$ decay with a branching ratio of 100%. The excluded regions from previous publications [19, 24] (gray shaded area) are obtained under the hypothesis of mostly-right-handed stops, while new results are obtained with an unpolarized signal assumption.

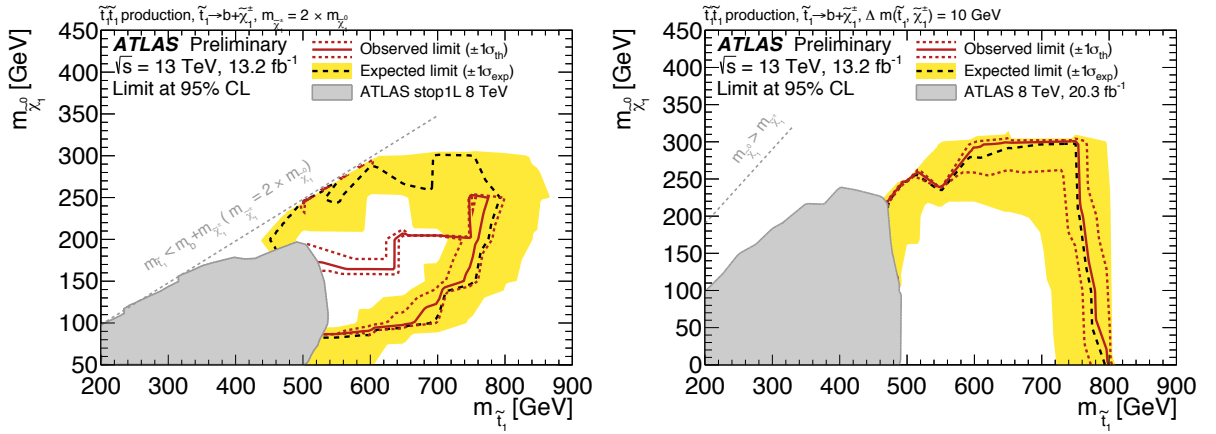


Figure 12: Expected (black dashed) and observed (red solid) 95% excluded regions in the plane of $m_{\tilde{t}_1}$ versus $m_{\tilde{\chi}_1^0}$ for direct stop pair production assuming $b\tilde{\chi}_1^\pm$ decay with a branching ratio of 100%. The chargino mass is assumed to be twice the neutralino mass (left) or close to the stop mass, $m_{\tilde{\chi}_1^\pm} = m_{\tilde{t}_1} - 10$ GeV (right). The excluded regions (gray shaded area) from previous publications, stop search in the one-lepton channel at 8 TeV (left) [24] and ATLAS stop search at 8 TeV (right) [25], are obtained under the hypothesis of mostly-left-handed stops, while new results are obtained with an unpolarized signal assumption.

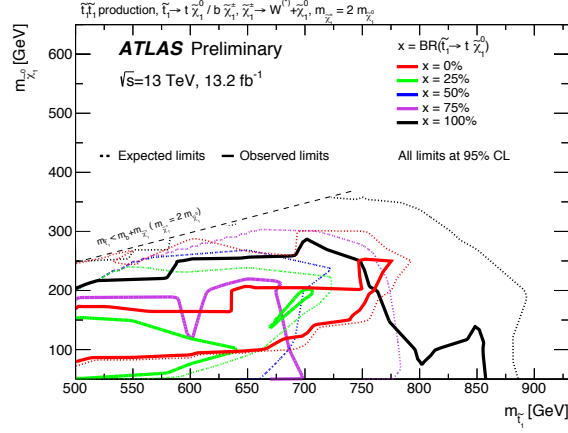


Figure 13: Expected (dashed) and observed (solid) 95% excluded regions in the plane of $m_{\tilde{t}_1}$ versus $m_{\tilde{\chi}_1^0}$ for direct stop pair production for different assumptions of $x = \mathcal{BR}(\tilde{t}_1 \rightarrow t + \tilde{\chi}_1^0) = 1 - \mathcal{BR}(\tilde{t}_1 \rightarrow b + \tilde{\chi}_1^\pm)$ where the chargino mass is assumed to be twice the neutralino mass, and x is scanned from 0% to 100% in steps of 25%. No points can be excluded in data for the $x = 50\%$ scenario.

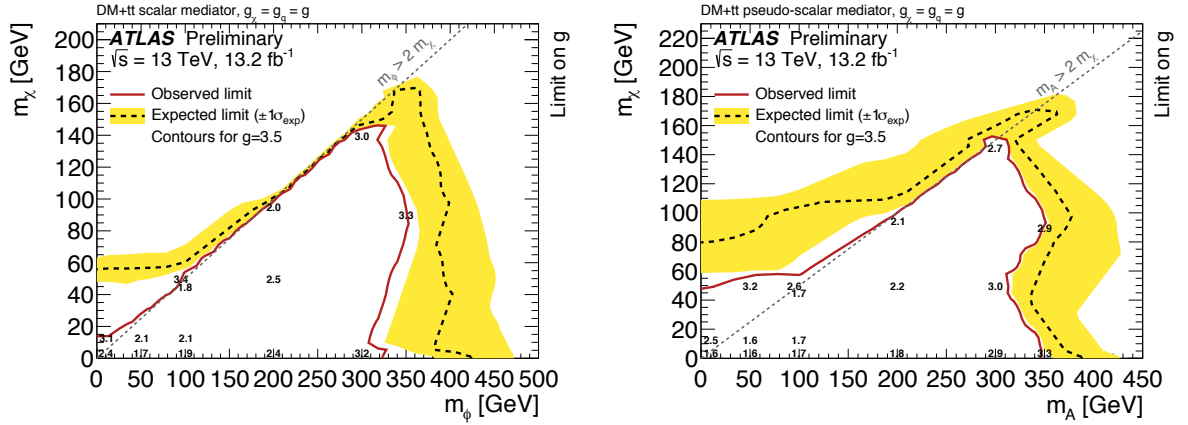


Figure 14: The observed upper limit on the couplings in the plane of m_{Med} versus m_{χ} for dark matter associated production with top quarks for a scalar mediator (left) and pseudo-scalar mediator (right). The observed and expected lines correspond to the limit for the coupling $g = 3.5$. Numbers on the plot show the value of the coupling. The coupling being shown and the coupling above are excluded at 95% CL for the corresponding points on the signal grid.

9 Conclusion

This note presents a search for direct pair production of stops decaying to two top quarks and two lightest neutralinos or two b quarks and two charginos in the final state with one isolated lepton, jets, and missing transverse momentum. Five signal region selections are optimized for the discovery of the stop signature. The analysis also defines two signal region selections for a dark matter motivated signature with the same $t\bar{t} + E_{\text{T}}^{\text{miss}}$ final state. The search uses 13.2 fb^{-1} of LHC pp collision data collected by the ATLAS experiment at a center-of-mass energy of $\sqrt{s} = 13 \text{ TeV}$. The largest difference between data and the SM prediction is found in the DM_low SR, corresponding to 3.3 standard deviations above the estimated background. Exclusion limits at 95% CL are derived for stop pair production models and dark matter produced in association with top quarks. For the direct stop pair production models the results extend previous exclusion limits by excluding the stop mass region up to 830 GeV for a massless lightest neutralino under the assumption of $\mathcal{BR}(\tilde{t}_1 \rightarrow t + \tilde{\chi}_1^0) = 100\%$. Exclusion limits are also extended in stop pair production models with $\mathcal{BR}(\tilde{t}_1 \rightarrow b + \tilde{\chi}_1^\pm) = 100\%$ under different hypotheses of the mass splitting between the lightest neutralino and chargino. Limits are also placed in scenarios where both the $\tilde{t}_1 \rightarrow t + \tilde{\chi}_1^0$ and $\tilde{t}_1 \rightarrow b + \tilde{\chi}_1^\pm$ decay modes are allowed under the assumption of $m_{\tilde{\chi}_1^\pm} = 2m_{\tilde{\chi}_1^0}$. For the dark matter models the exclusion limits are obtained on the common coupling, g , under the assumption of a scalar or pseudo-scalar mediator. The maximal coupling of $g = 3.5$ is excluded at 95% confidence level for a scalar (pseudo-scalar) mediator mass up to 320 (350) GeV assuming a 1 GeV dark matter particle mass.

Appendix

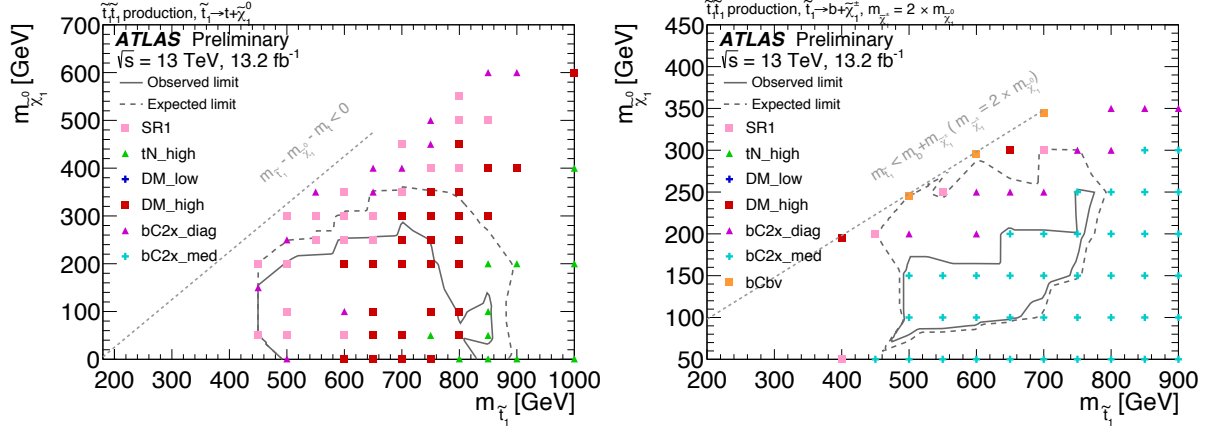


Figure 15: Illustration of the best expected signal region per signal grid point in the plane of $m_{\tilde{t}_1}$ versus $m_{\tilde{\chi}_1^0}$ for direct stop pair production assuming $t\tilde{\chi}_1^0$ ($b\tilde{\chi}_1^\pm$) decay with a branching ratio of 100% on the left (right). These mappings are used for the final combined exclusion limits.

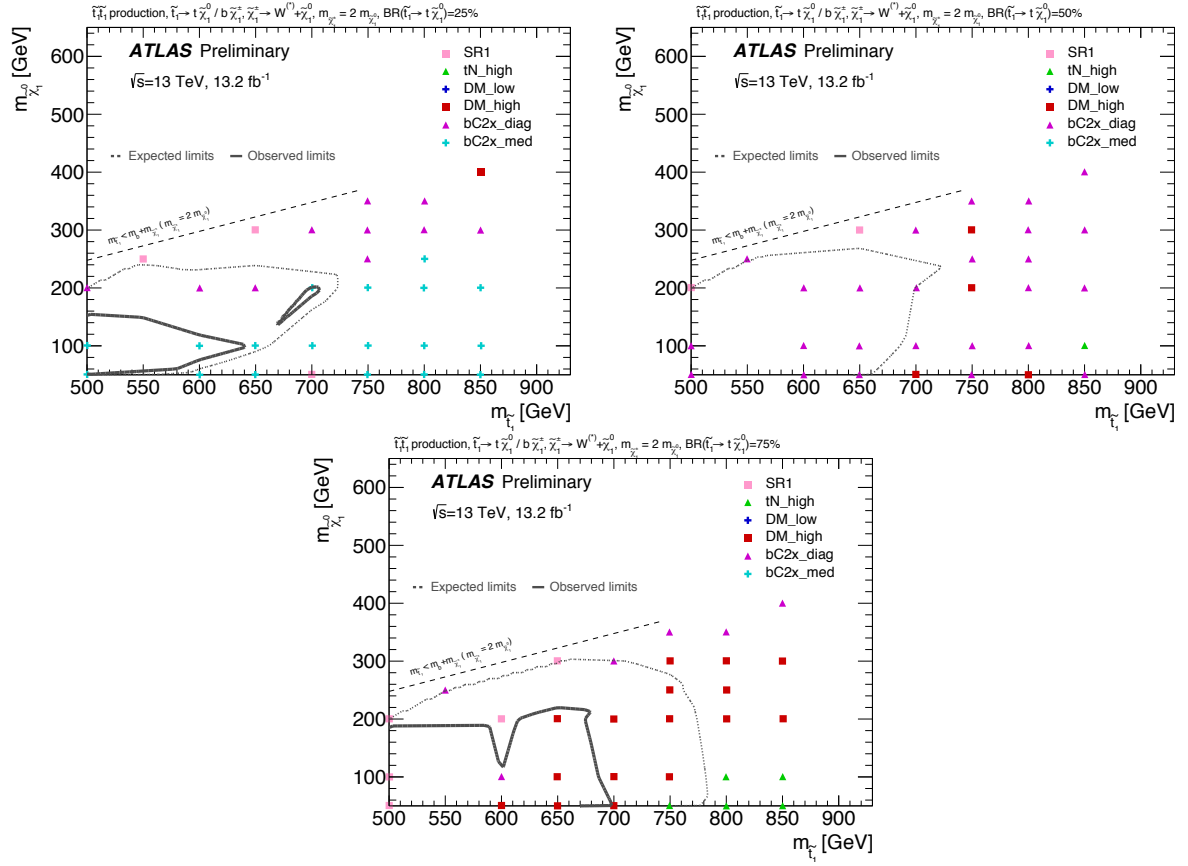


Figure 16: Illustration of the best expected signal region per signal grid point in the plane of $m_{\tilde{t}_1}$ versus $m_{\tilde{\chi}_1^0}$ for direct stop pair production assuming $x = \mathcal{BR}(\tilde{t}_1 \rightarrow t + \tilde{\chi}_1^0) = 1 - \mathcal{BR}(\tilde{t}_1 \rightarrow b + \tilde{\chi}_1^\pm)$. The chargino mass is assumed to be twice the neutralino mass and x varies from 0% to 100% in steps of 25%. The top left is for $\mathcal{BR}(\tilde{t}_1 \rightarrow t + \tilde{\chi}_1^0) = 25\%$, the top right for $\mathcal{BR}(\tilde{t}_1 \rightarrow t + \tilde{\chi}_1^0) = 50\%$, and the bottom for $\mathcal{BR}(\tilde{t}_1 \rightarrow t + \tilde{\chi}_1^0) = 75\%$.

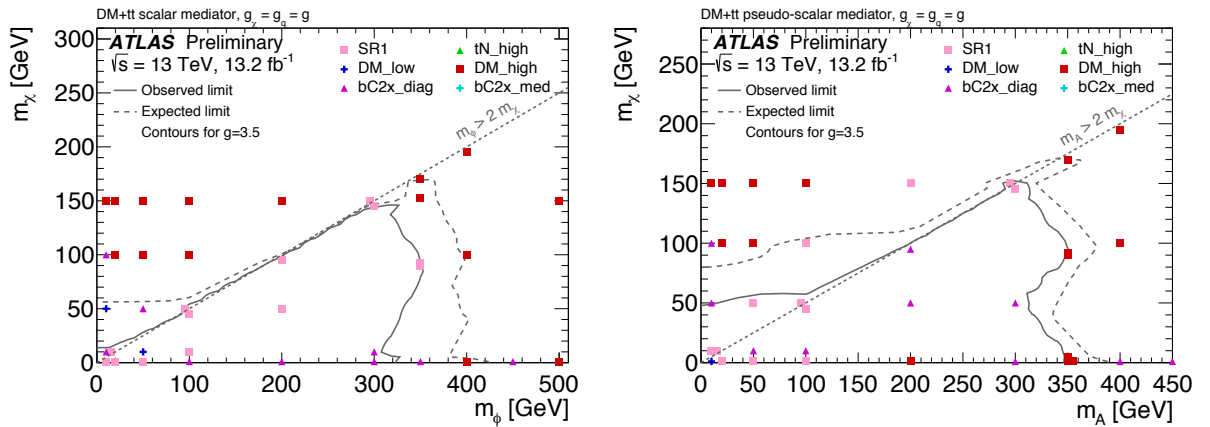


Figure 17: Illustration of the best expected signal region per signal grid point in the plane of m_{ϕ} (m_A) versus $m_{\tilde{\chi}}$ for dark matter production associated with top quarks for a scalar mediator (left) and pseudo-scalar mediator (right).

References

- [1] Yu. A. Golfand and E. P. Likhtman, *Extension of the Algebra of Poincare Group Generators and Violation of p Invariance*, JETP Lett. **13** (1971) 323, [Pisma Zh. Eksp. Teor. Fiz.13,452(1971)].
- [2] D. V. Volkov and V. P. Akulov, *Is the Neutrino a Goldstone Particle?* Phys. Lett. B **46** (1973) 109.
- [3] J. Wess and B. Zumino, *Supergauge Transformations in Four-Dimensions*, Nucl. Phys. B **70** (1974) 39.
- [4] J. Wess and B. Zumino, *Supergauge Invariant Extension of Quantum Electrodynamics*, Nucl. Phys. B **78** (1974) 1.
- [5] S. Ferrara and B. Zumino, *Supergauge Invariant Yang-Mills Theories*, Nucl. Phys. B **79** (1974) 413.
- [6] A. Salam and J. A. Strathdee, *Supersymmetry and Nonabelian Gauges*, Phys. Lett. B **51** (1974) 353.
- [7] R. Barbieri and G. F. Giudice, *Upper Bounds on Supersymmetric Particle Masses*, Nucl. Phys. B **306** (1988) 63.
- [8] B. de Carlos and J. A. Casas, *One loop analysis of the electroweak breaking in supersymmetric models and the fine tuning problem*, Phys. Lett. B **309** (1993) 320, arXiv: [hep-ph/9303291](#) [hep-ph].
- [9] N. Sakai, *Naturalness in Supersymmetric Guts*, Z. Phys. C **11** (1981) 153.
- [10] S. Dimopoulos, S. Raby, and F. Wilczek, *Supersymmetry and the Scale of Unification*, Phys. Rev. D **24** (1981) 1681.
- [11] L. E. Ibanez and G. G. Ross, *Low-Energy Predictions in Supersymmetric Grand Unified Theories*, Phys. Lett. B **105** (1981) 439.
- [12] S. Dimopoulos and H. Georgi, *Softly Broken Supersymmetry and $SU(5)$* , Nucl. Phys. B **193** (1981) 150.
- [13] K. Inoue et al., *Aspects of Grand Unified Models with Softly Broken Supersymmetry*, Prog. Theor. Phys. **68** (1982) 927, [Erratum: Prog. Theor. Phys.70,330(1983)].
- [14] J. R. Ellis and S. Rudaz, *Search for Supersymmetry in Toponium Decays*, Phys. Lett. B **128** (1983) 248.
- [15] K. Abe et al., *Search for proton decay via $p \rightarrow \nu K^+$ using 260 kiloton-year data of Super-Kamiokande*, Phys. Rev. D **90** (2014) 072005, arXiv: [1408.1195](#) [hep-ex].
- [16] G. R. Farrar and P. Fayet, *Phenomenology of the Production, Decay, and Detection of New Hadronic States Associated with Supersymmetry*, Phys. Lett. B **76** (1978) 575.
- [17] H. Goldberg, *Constraint on the Photino Mass from Cosmology*, Phys. Rev. Lett. **50** (1983) 1419, [Erratum: Phys. Rev. Lett.103,099905(2009)].
- [18] J. R. Ellis et al., *Supersymmetric Relics from the Big Bang*, Nucl. Phys. B **238** (1984) 453.

- [19] ATLAS Collaboration, *Search for top squarks in final states with one isolated lepton, jets, and missing transverse momentum in $\sqrt{s} = 13$ TeV pp collisions with the ATLAS detector*, (2016), arXiv: [1606.03903 \[hep-ex\]](#).
- [20] D. Abercrombie et al, *Dark Matter Benchmark Models for Early LHC Run-2 Searches: Report of the ATLAS/CMS Dark Matter Forum*, (2015), arXiv: [1507.00966 \[hep-ex\]](#).
- [21] M.R. Buckley, D. Feld, and D. Goncalves, *Scalar Simplified Models for Dark Matter*, *Phys. Rev. D* **91** (2015) 015017, arXiv: [1410.6497 \[hep-ph\]](#).
- [22] U. Haisch and E. Re, *Simplified dark matter top-quark interactions at the LHC*, *JHEP* **06** (2015) 078, arXiv: [1503.00691 \[hep-ph\]](#).
- [23] ATLAS Collaboration, *Search for direct top squark pair production in final states with one isolated lepton, jets, and missing transverse momentum in $\sqrt{s} = 7$ TeV pp collisions using 4.7 fb^{-1} of ATLAS data*, *Phys. Rev. Lett.* **109** (2012) 211803, arXiv: [1208.2590 \[hep-ex\]](#).
- [24] ATLAS Collaboration, *Search for top squark pair production in final states with one isolated lepton, jets, and missing transverse momentum in $\sqrt{s} = 8$ TeV pp collisions with the ATLAS detector*, *JHEP* **1411** (2014) 118, arXiv: [1407.0583 \[hep-ex\]](#).
- [25] ATLAS Collaboration, *ATLAS Run 1 searches for direct pair production of third-generation squarks at the Large Hadron Collider*, *Eur. Phys. J. C* **75** (2015) 510, arXiv: [1506.08616 \[hep-ex\]](#).
- [26] CMS Collaboration, *Searches for third-generation squark production in fully hadronic final states in proton–proton collisions at $\sqrt{s} = 8$ TeV*, *JHEP* **1506** (2015) 116, arXiv: [1503.08037 \[hep-ex\]](#).
- [27] CMS Collaboration, *Search for direct pair production of scalar top quarks in the single- and dilepton channels in proton-proton collisions at $\sqrt{s} = 8$ TeV*, (2016), arXiv: [1602.03169 \[hep-ex\]](#).
- [28] CMS Collaboration, *Search for top-squark pair production in the single-lepton final state in pp collisions at $\sqrt{s} = 8$ TeV*, *Eur. Phys. J. C* **73** (2013) 2677, arXiv: [1308.1586 \[hep-ex\]](#).
- [29] CMS Collaboration, *Search for supersymmetry using razor variables in events with b-tagged jets in pp collisions at $\sqrt{s} = 8$ TeV*, *Phys. Rev. D* **91** (2015) 052018, arXiv: [1502.00300 \[hep-ex\]](#).
- [30] CMS Collaboration, *Searches for supersymmetry using the M_{T2} variable in hadronic events produced in pp collisions at 8 TeV*, *JHEP* **1505** (2015) 078, arXiv: [1502.04358 \[hep-ex\]](#).
- [31] CMS Collaboration, *Search for new physics with the $MT2$ variable in all-jets final states produced in pp collisions at $\sqrt{s} = 13$ TeV*, (2016), arXiv: [1603.04053 \[hep-ex\]](#).
- [32] ATLAS Collaboration, *Search for dark matter in events with heavy quarks and missing transverse momentum in pp collisions with the ATLAS detector*, *Eur. Phys. J. C* **75** (2015) 92, arXiv: [1410.4031 \[hep-ex\]](#).
- [33] CMS Collaboration, *Search for the production of dark matter in association with top-quark pairs in the single-lepton final state in proton–proton collisions at $\sqrt{s} = 8$ TeV*, *JHEP* **1506** (2015) 121, arXiv: [1504.03198 \[hep-ex\]](#).
- [34] ATLAS Collaboration, *The ATLAS Experiment at the CERN Large Hadron Collider*, *JINST* **3** (2008) S08003.

- [35] ATLAS Collaboration,
Early Inner Detector Tracking Performance in the 2015 Data at $\sqrt{s} = 13$ TeV,
ATL-PHYS-PUB-2015-051, 2015, URL: <http://cdsweb.cern.ch/record/2110140>.
- [36] ATLAS Collaboration, *Improved luminosity determination in pp collisions at $\sqrt{s} = 7$ TeV using the ATLAS detector at the LHC*, *Eur. Phys. J. C* **73** (2013) 2518, arXiv: [1302.4393 \[hep-ex\]](#).
- [37] ATLAS Collaboration,
Luminosity determination in pp collisions at $\sqrt{s} = 8$ TeV using the ATLAS detector at the LHC,
to be submitted to *Eur. Phys. J.* ().
- [38] J. Alwall et al., *The automated computation of tree-level and next-to-leading order differential cross sections, and their matching to parton shower simulations*, *JHEP* **1407** (2014) 079, arXiv: [1405.0301 \[hep-ph\]](#).
- [39] T. Sjöstrand, S. Mrenna, and P. Z. Skands, *A Brief Introduction to PYTHIA 8.1*, *Comput. Phys. Commun.* **178** (2008) 852, arXiv: [0710.3820 \[hep-ph\]](#).
- [40] L. Lönnblad and S. Prestel, *Matching Tree-Level Matrix Elements with Interleaved Showers*, *JHEP* **1203** (2012) 019, arXiv: [1109.4829 \[hep-ph\]](#).
- [41] S. Frixione and B. R. Webber,
Matching NLO QCD computations and parton shower simulations, *JHEP* **06** (2002) 029, arXiv: [hep-ph/0204244](#).
- [42] S. Alioli et al., *A general framework for implementing NLO calculations in shower Monte Carlo programs: the POWHEG BOX*, *JHEP* **1006** (2010) 043, arXiv: [1002.2581 \[hep-ph\]](#).
- [43] E. Re,
Single-top Wt-channel production matched with parton showers using the POWHEG method, *Eur. Phys. J. C* **71** (2011) 1547, arXiv: [1009.2450 \[hep-ph\]](#).
- [44] S. Frixione, P. Nason, and G. Ridolfi,
A Positive-weight next-to-leading-order Monte Carlo for heavy flavour hadroproduction, *JHEP* **0709** (2007) 126, arXiv: [0707.3088 \[hep-ph\]](#).
- [45] R. Frederix, E. Re, and P. Torrielli, *Single-top t-channel hadroproduction in the four-flavour scheme with POWHEG and aMC@NLO*, *JHEP* **1209** (2012) 130, arXiv: [1207.5391 \[hep-ph\]](#).
- [46] S. Alioli et al.,
NLO single-top production matched with shower in POWHEG: s- and t-channel contributions, *JHEP* **0909** (2009) 111, [Erratum: *JHEP*02,011(2010)], arXiv: [0907.4076 \[hep-ph\]](#).
- [47] T. Sjöstrand, S. Mrenna, and P. Z. Skands, *PYTHIA 6.4 Physics and Manual*, *JHEP* **0605** (2006) 026, arXiv: [hep-ph/0603175](#).
- [48] P. Nason, *A New method for combining NLO QCD with shower Monte Carlo algorithms*, *JHEP* **0411** (2004) 040, arXiv: [hep-ph/0409146 \[hep-ph\]](#).
- [49] S. Frixione, P. Nason, and C. Oleari,
Matching NLO QCD computations with Parton Shower simulations: the POWHEG method, *JHEP* **0711** (2007) 070, arXiv: [0709.2092 \[hep-ph\]](#).
- [50] T. Gleisberg et al., *Event generation with SHERPA 1.1*, *JHEP* **0902** (2009) 007, arXiv: [0811.4622 \[hep-ph\]](#).
- [51] T. Gleisberg and S. Höche, *Comix, a new matrix element generator*, *JHEP* **0812** (2008) 039, arXiv: [0808.3674 \[hep-ph\]](#).

- [52] F. Cascioli, P. Maierhofer, and S. Pozzorini, *Scattering Amplitudes with Open Loops*, *Phys. Rev. Lett.* **108** (2012) 111601, arXiv: [1111.5206 \[hep-ph\]](#).
- [53] S. Schumann and F. Krauss, *A Parton shower algorithm based on Catani-Seymour dipole factorisation*, *JHEP* **0803** (2008) 038, arXiv: [0709.1027 \[hep-ph\]](#).
- [54] H.-L. Lai et al., *New parton distributions for collider physics*, *Phys. Rev. D* **82** (2010) 074024, arXiv: [1007.2241 \[hep-ph\]](#).
- [55] R. D. Ball et al., *Parton distributions for the LHC Run II*, *JHEP* **1504** (2015) 040, arXiv: [1410.8849 \[hep-ph\]](#).
- [56] R. D. Ball et al., *Parton distributions with LHC data*, *Nucl. Phys. B* **867** (2013) 244, arXiv: [1207.1303 \[hep-ph\]](#).
- [57] J. Pumplin et al., *New generation of parton distributions with uncertainties from global QCD analysis*, *JHEP* **0207** (2002) 012, arXiv: [hep-ph/0201195 \[hep-ph\]](#).
- [58] P. Z. Skands, *Tuning Monte Carlo Generators: The Perugia Tunes*, *Phys. Rev. D* **82** (2010) 074018, arXiv: [1005.3457 \[hep-ph\]](#).
- [59] ATLAS Collaboration, *ATLAS Pythia 8 tunes to 7 TeV data*, ATL-PHYS-PUB-2014-021, 2014, URL: <http://cdsweb.cern.ch/record/1966419>.
- [60] D. J. Lange, *The EvtGen particle decay simulation package*, *Nucl. Instrum. Meth. A* **462** (2001) 152.
- [61] ATLAS Collaboration, *Studies on the MC generator modelling of top pair and single top (Wt) processes as used in Run2*, ATL-PHYS-PUB-2016-004, 2016, URL: <http://cdsweb.cern.ch/record/2120417>.
- [62] ATLAS Collaboration, *Monte Carlo Generators for the Production of a W or Z/γ^* Boson in Association with Jets at ATLAS in Run 2*, ATL-PHYS-PUB-2016-003, 2016, URL: <http://cdsweb.cern.ch/record/2120133>.
- [63] ATLAS Collaboration, *Studies on the MC generator modelling of ttX ($X=W,Z,\text{gamma},\text{Higgs or heavy flavor jets}$) processes as used in Run2*, ATL-PHYS-PUB-2016-005, 2016, URL: <http://cds.cern.ch/record/2120826>.
- [64] ATLAS Collaboration, *Multi-boson simulation for 13 TeV ATLAS analyses*, ATL-PHYS-PUB-2016-002, 2016, URL: <http://cdsweb.cern.ch/record/2119986>.
- [65] M. Czakon, P. Fiedler, and A. Mitov, *Total Top-Quark Pair-Production Cross Section at Hadron Colliders Through $O(\alpha_S^4)$* , *Phys. Rev. Lett.* **110** (2013) 252004, arXiv: [1303.6254 \[hep-ph\]](#).
- [66] M. Czakon and A. Mitov, *NNLO corrections to top pair production at hadron colliders: the quark-gluon reaction*, *JHEP* **1301** (2013) 080, arXiv: [1210.6832 \[hep-ph\]](#).
- [67] M. Czakon and A. Mitov, *NNLO corrections to top-pair production at hadron colliders: the all-fermionic scattering channels*, *JHEP* **1212** (2012) 054, arXiv: [1207.0236 \[hep-ph\]](#).
- [68] P. Baernreuther, M. Czakon, and A. Mitov, *Percent Level Precision Physics at the Tevatron: First Genuine NNLO QCD Corrections to $q\bar{q} \rightarrow t\bar{t} + X$* , *Phys. Rev. Lett.* **109** (2012) 132001, arXiv: [1204.5201 \[hep-ph\]](#).

- [69] M. Cacciari et al., *Top-pair production at hadron colliders with next-to-next-to-leading logarithmic soft-gluon resummation*, *Phys. Lett. B* **710** (2012) 612, arXiv: [1111.5869 \[hep-ph\]](#).
- [70] M. Czakon and A. Mitov, *Top++: A Program for the Calculation of the Top-Pair Cross-Section at Hadron Colliders*, *Comput. Phys. Commun.* **185** (2014) 2930, arXiv: [1112.5675 \[hep-ph\]](#).
- [71] N. Kidonakis, *Next-to-next-to-leading-order collinear and soft gluon corrections for t-channel single top quark production*, *Phys. Rev. D* **83** (2011) 091503, arXiv: [1103.2792 \[hep-ph\]](#).
- [72] N. Kidonakis, *Two-loop soft anomalous dimensions for single top quark associated production with a W- or H-*, *Phys. Rev. D* **82** (2010) 054018, arXiv: [1005.4451 \[hep-ph\]](#).
- [73] N. Kidonakis, *NNLL resummation for s-channel single top quark production*, *Phys. Rev. D* **81** (2010) 054028, arXiv: [1001.5034 \[hep-ph\]](#).
- [74] S. Catani et al., *Vector boson production at hadron colliders: a fully exclusive QCD calculation at NNLO*, *Phys. Rev. Lett.* **103** (2009) 082001, arXiv: [0903.2120 \[hep-ph\]](#).
- [75] C. Borschensky et al., *Squark and gluino production cross sections in pp collisions at $\sqrt{s} = 13, 14, 33$ and 100 TeV*, *Eur. Phys. J. C* **74** (2014) 3174, arXiv: [1407.5066 \[hep-ph\]](#).
- [76] K. Melnikov, M. Schulze, and A. Scharf, *QCD corrections to top quark pair production in association with a photon at hadron colliders*, *Phys. Rev. D* **83** (2011) 074013, arXiv: [1102.1967 \[hep-ph\]](#).
- [77] ATLAS Collaboration, *The ATLAS Simulation Infrastructure*, *Eur. Phys. J. C* **70** (2010) 823, arXiv: [1005.4568 \[hep-ex\]](#).
- [78] S. Agostinelli et al. (GEANT4 Collaboration), *GEANT4: A Simulation toolkit*, *Nucl. Instrum. Meth. A* **506** (2003) 250.
- [79] ATLAS Collaboration, *The simulation principle and performance of the ATLAS fast calorimeter simulation FastCaloSim*, ATL-PHYS-PUB-2010-013, 2010, URL: <http://cds.cern.ch/record/1300517>.
- [80] ATLAS Collaboration, *Electron identification measurements in ATLAS using $\sqrt{s} = 13$ TeV data with 50 ns bunch spacing*, ATL-PHYS-PUB-2015-041, 2015, URL: <http://cdsweb.cern.ch/record/2048202>.
- [81] “Electron efficiency measurements with the ATLAS detector using the 2015 LHC proton-proton collision data,” tech. rep. ATLAS-CONF-2016-024, CERN, 2016, URL: <https://cds.cern.ch/record/2157687>.
- [82] ATLAS Collaboration, *Muon reconstruction performance of the ATLAS detector in proton-proton collision data at $\sqrt{s} = 13$ TeV*, *Eur. Phys. J. C* **76** (2016) 292, arXiv: [1603.05598 \[hep-ex\]](#).
- [83] ATLAS Collaboration, *Expected photon performance in the ATLAS experiment*, ATL-PHYS-PUB-2011-007, 2011, URL: <http://cdsweb.cern.ch/record/1345329>.
- [84] W. Lampl et al., *Calorimeter Clustering Algorithms: Description and Performance*, ATL-LARG-PUB-2008-002, 2008, URL: <http://cds.cern.ch/record/1099735>.

- [85] ATLAS Collaboration, *Jet energy measurement with the ATLAS detector in proton–proton collisions at $\sqrt{s} = 7$ TeV*, *Eur. Phys. J. C* **73** (2013) 2304, arXiv: [1112.6426 \[hep-ex\]](#).
- [86] M. Cacciari, G. P. Salam, and G. Soyez, *The Anti- $k(t)$ jet clustering algorithm*, *JHEP* **0804** (2008) 063, arXiv: [0802.1189 \[hep-ph\]](#).
- [87] M. Cacciari and G. P. Salam, *Pileup subtraction using jet areas*, *Phys. Lett. B* **659** (2008) 119, arXiv: [0707.1378 \[hep-ph\]](#).
- [88] M. Cacciari, G. P. Salam, and G. Soyez, *The Catchment Area of Jets*, *JHEP* **0804** (2008) 005, arXiv: [0802.1188 \[hep-ph\]](#).
- [89] ATLAS Collaboration, *Performance of pile-up mitigation techniques for jets in pp collisions at $\sqrt{s} = 8$ TeV using the ATLAS detector*, *Nucl. Instrum. Meth. A* **824** (2016) 367, arXiv: [1510.03823 \[hep-ex\]](#).
- [90] ATLAS Collaboration, *Jet energy measurement and its systematic uncertainty in proton–proton collisions at $\sqrt{s} = 7$ TeV with the ATLAS detector*, *Eur. Phys. J. C* **75** (2015) 17, arXiv: [1406.0076 \[hep-ex\]](#).
- [91] ATLAS Collaboration, *Jet Calibration and Systematic Uncertainties for Jets Reconstructed in the ATLAS Detector at $\sqrt{s} = 13$ TeV*, ATL-PHYS-PUB-2015-015, 2015, URL: <http://cds.cern.ch/record/2037613>.
- [92] ATLAS Collaboration, *Characterisation and mitigation of beam-induced backgrounds observed in the ATLAS detector during the 2011 proton–proton run*, *JINST* **8** (2013) P07004, arXiv: [1303.0223 \[hep-ex\]](#).
- [93] ATLAS Collaboration, *Selection of jets produced in 13 TeV proton–proton collisions with the ATLAS detector*, ATLAS-CONF-2015-029, 2015, URL: <http://cdsweb.cern.ch/record/2037702>.
- [94] ATLAS Collaboration, “Optimisation of the ATLAS b -tagging performance for the 2016 LHC Run,” tech. rep. ATL-PHYS-PUB-2016-012, CERN, 2016, URL: <https://cds.cern.ch/record/2160731>.
- [95] ATLAS Collaboration, *Performance of b -Jet Identification in the ATLAS Experiment*, *JINST* **11** (2016) P04008, arXiv: [1512.01094 \[hep-ex\]](#).
- [96] ATLAS Collaboration, *Commissioning of the reconstruction of hadronic tau lepton decays in ATLAS using pp collisions at $\sqrt{s} = 13$ TeV*, ATL-PHYS-PUB-2015-025, 2015, URL: <http://cdsweb.cern.ch/record/2037716>.
- [97] ATLAS Collaboration, *Reconstruction, Energy Calibration, and Identification of Hadronically Decaying Tau Leptons in the ATLAS Experiment for Run-2 of the LHC*, ATL-PHYS-PUB-2015-045, 2015, URL: <http://cds.cern.ch/record/2064383>.
- [98] ATLAS Collaboration, *Performance of missing transverse momentum reconstruction with the ATLAS detector in the first proton–proton collisions at $\sqrt{s} = 13$ TeV*, ATL-PHYS-PUB-2015-027, 2015, URL: <http://cdsweb.cern.ch/record/2037904>.
- [99] ATLAS Collaboration, *Expected performance of missing transverse momentum reconstruction for the ATLAS detector at $\sqrt{s} = 13$ TeV*, ATL-PHYS-PUB-2015-023, 2015, URL: <http://cdsweb.cern.ch/record/2037700>.

- [100] ATLAS Collaboration, *Search for new phenomena in final states with large jet multiplicities and missing transverse momentum at $\sqrt{s} = 8$ TeV proton–proton collisions using the ATLAS experiment*, [JHEP **1310** \(2013\) 130](#), arXiv: [1308.1841 \[hep-ex\]](#).
- [101] ATLAS Collaboration, *Search for direct pair production of the top squark in all-hadronic final states in proton–proton collisions at $\sqrt{s} = 8$ TeV with the ATLAS detector*, [JHEP **1409** \(2014\) 015](#), arXiv: [1406.1122 \[hep-ex\]](#).
- [102] B. Nachman et al., *Jets from Jets: Re-clustering as a tool for large radius jet reconstruction and grooming at the LHC*, [JHEP **1502** \(2015\) 075](#), arXiv: [1407.2922 \[hep-ph\]](#).
- [103] D. Krohn, J. Thaler, and L.-T. Wang, *Jet Trimming*, [JHEP **1002** \(2010\) 084](#), arXiv: [0912.1342 \[hep-ph\]](#).
- [104] B. Nachman and C. G. Lester, *Significance Variables*, [Phys. Rev. D **88** \(2013\) 075013](#), arXiv: [1303.7009 \[hep-ph\]](#).
- [105] A. J. Barr, B. Gripaios, and C. G. Lester, *Transverse masses and kinematic constraints: from the boundary to the crease*, [JHEP **0911** \(2009\) 096](#), arXiv: [0908.3779 \[hep-ph\]](#).
- [106] P. Konar et al., *Dark Matter Particle Spectroscopy at the LHC: Generalizing $M(T_2)$ to Asymmetric Event Topologies*, [JHEP **1004** \(2010\) 086](#), arXiv: [0911.4126 \[hep-ph\]](#).
- [107] Y. Bai et al., *Stop the Top Background of the Stop Search*, [JHEP **1207** \(2012\) 110](#), arXiv: [1203.4813 \[hep-ph\]](#).
- [108] C. G. Lester and B. Nachman, *Bisection-based asymmetric M_{T2} computation: a higher precision calculator than existing symmetric methods*, [JHEP **1503** \(2015\) 100](#), arXiv: [1411.4312 \[hep-ph\]](#).
- [109] C. G. Lester and D. J. Summers, *Measuring masses of semi-invisibly decaying particles pair produced at hadron colliders*, [Phys. Lett. B **463** \(1999\) 99](#), arXiv: [hep-ph/9906349 \[hep-ph\]](#).
- [110] M. L. Graesser and J. Shelton, *Hunting Mixed Top Squark Decays*, [Phys. Rev. Lett. **111** \(2013\) 121802](#), arXiv: [1212.4495 \[hep-ph\]](#).
- [111] M. Baak et al., *HistFitter software framework for statistical data analysis*, [Eur. Phys. J. C **75** \(2015\) 153](#), arXiv: [1410.1280 \[hep-ex\]](#).
- [112] ATLAS Collaboration, *Calibration of b -tagging using dileptonic top pair events in a combinatorial likelihood approach with the ATLAS experiment*, ATLAS-CONF-2014-004, 2014, URL: <http://cdsweb.cern.ch/record/1664335>.
- [113] ATLAS Collaboration, *Calibration of the performance of b -tagging for c and light-flavour jets in the 2012 ATLAS data*, ATLAS-CONF-2014-046, 2014, URL: <http://cdsweb.cern.ch/record/1741020>.
- [114] S. Dulat et al., *New parton distribution functions from a global analysis of quantum chromodynamics*, [Phys. Rev. D **93** \(2016\) 033006](#), arXiv: [1506.07443 \[hep-ph\]](#).
- [115] ATLAS Collaboration, *Measurement of the cross-section for W boson production in association with b -jets in pp collisions at $\sqrt{s} = 7$ TeV with the ATLAS detector*, [JHEP **1306** \(2013\) 084](#), arXiv: [1302.2929 \[hep-ex\]](#).

- [116] M. Kramer et al., *Supersymmetry production cross sections in pp collisions at $\sqrt{s} = 7$ TeV*, (2012), arXiv: [1206.2892 \[hep-ph\]](#).
- [117] A. L. Read, *Presentation of search results: the CL_s technique*, J. Phys. G **28** (2002) 2693, URL: <https://cds.cern.ch/record/722145>.